



MSC APPLIED MATHEMATICS PROJECT
2017/2018

IMPERIAL COLLEGE LONDON
DEPARTMENT OF MATHEMATICS

**An Advanced Numerical Algorithm
for the Simulation of Weather Fronts**

Author:

Chloe Raymont

CID:

00733439

Supervisor:

Dr. Colin Cotter

September 12, 2018

Abstract

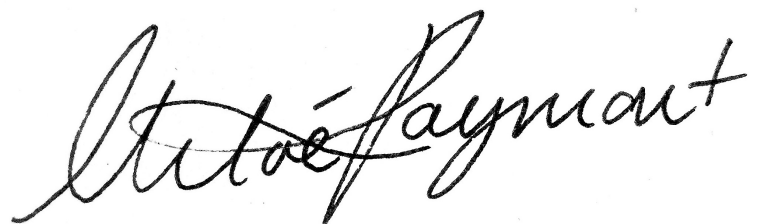
This project studies the growth of a baroclinic instability responsible for the formation of weather fronts in the atmosphere. A model is developed using the semi-geostrophic equations introduced by Hoskins [1] by means of co-ordinate transform. A development of the transformation by Shutts and Cullen [2] leads to a form of the semi-geostrophic equations which can be reformulated as an optimal transport problem where the energy is the cost to be minimised [3]. This is shown to be equivalent to an optimal transport problem minimising a quadratic cost. In this form we show that the Damped Newton Algorithm developed by Kitawaga et al. [4, 5], and shown to be particularly efficient for solving such problems, can be applied. Numerical error and performance are subsequently analysed to validate results.

Acknowledgements

I would like to thank my supervisor Dr Colin Cotter for his valuable support and guidance throughout this project. Particularly for proposing such an enjoyable and compelling subject area to study. I would also like to thank his colleagues for their suggestions and advice. I would also like to acknowledge the support of my friends and family throughout my studies.

Declaration

The work contained in this project is my own work unless otherwise stated.

A handwritten signature in black ink, appearing to read "Stéphanie Pommerehne". The signature is fluid and cursive, with "Stéphanie" on top and "Pommerehne" on the bottom, though the two names are somewhat interconnected in the script.

Contents

Introduction	7
1 The Governing Equations	9
1.1 The 3D Incompressible Boussinesq Equations	10
1.2 The Vertical Slice Model	11
1.3 The Geostrophic Momentum Approximation	12
2 The Frontogenesis Model as an Optimal Transport Problem	15
2.1 The Semi-Geostrophic Equations	15
2.2 Energy Minimisation as an Optimal Transportation Problem	17
2.2.1 Finding an Inverse Transformation	17
2.2.2 The Monge-Ampère equation and Optimal Transportation	18
3 Using Semi-discrete Optimal Transport to solve the Semi-Geostrophic Equations	22
3.1 Semi-discrete Optimal Transport	22
3.2 Laguerre Cells and the Inclusion of weights	24
3.3 Applying semi-discrete optimal transport to solving the semi-geostrophic equations	25
3.4 Extension for Periodic Boundary Conditions	26
3.4.1 Calculating Moments of a cell with Periodic Boundary Conditions	26
3.4.2 Mapping to the Fundamental Domain	28
3.5 Validating the application of DA to the system SG/EM	29
4 A Numerical Solution to the Eady Model for Frontogenesis	30
4.1 Algorithm for solving the semi-geostrophic Eady model for Frontogenesis	31
4.2 Initialisation of Points in Geostrophic Space	31
4.3 Choice of Initial Weights	32
4.4 Time Stepping	34
4.4.1 Forward-Euler Scheme	34

4.4.2	Heun's Method	35
4.5	Visualising the Output	35
5	Numerical Simulations and Results	37
5.1	Physical interpretation of Results	37
5.2	Total Energy as a Measurement of Error	43
5.3	A Comparison of Time Stepping Methods	50
5.4	Computational Performance	52
	Conclusion	55
	A First Appendix	57

List of Figures

1	Cold Front	8
2	Surface Pressure Chart from 12/09/2018	8
1.1	Local Cartesian co-ordinates (x, y, z) on Earth	9
2.1	Map from geostrophic points to fluid 'parcels'	19
3.1	Semi-discrete Optimal Transport	22
3.2	The partitioning of a Domain	23
3.3	Laguerre diagram produced by finding weights using DA for optimal transport	24
3.4	Optimal Transport with Periodic Boundary Conditions	27
3.5	Periodic boundary conditions with 'ghost' points	27
3.6	Plots of a random set of points initialised in $[0, 2] \times [0, 2]$ before (a) and after (b) being mapped to the fundamental domain $[0, 1] \times [0, 1]$.	28
4.1	Plot of Points in Geostrophic Space	33
4.2	Coloured Laguerre Diagram of Cells	35
5.1	Plots of Laguerre Diagrams shaded according to the value of θ' using a random mesh of 80×40 points initialised in geostrophic space using 4.2 at (a) 0 days, (b) 2.5 days (c) 6 days and (d) 9 days, $\Gamma = [-L, L] \times [0, H]$, where $L = 1 \times 10^6$ and $H = 1 \times 10^4$	39
5.2	Plots of Laguerre Diagrams shaded according to the value of θ' using a random mesh of 80×40 points initialised in geostrophic space using 4.2 at (a) 6 days, (b) 9 days, $\Gamma = [-L, L] \times [0, H]$, where $L = 1 \times 10^6$ and $H = 1 \times 10^4$	40
5.3	Plots of Laguerre Diagrams shaded according to the value of θ' using a random mesh of 80×40 points initialised in geostrophic space using 4.2 at (a) 11 days, (b) 12.5 days (c) 14.5 days, $\Gamma = [-L, L] \times [0, H]$, where $L = 1 \times 10^6$ and $H = 1 \times 10^4$	42
5.4	Plot of Geostrophic points at 11 days	43
5.5	Plot of Geostrophic points at 12.5 days	43

5.6	Plot of Geostrophic points at 14.5 days	43
5.7	Plot of Laguerre Diagrams shaded according to the value of v_g using a random mesh of 80×40 points initialised in geostrophic space using 4.2 at (a) 0 days and (b) 2.5 days , $\Gamma = [-L, L] \times [0, H]$, where $L = 1 \times 10^6$ and $H = 1 \times 10^4$	44
5.8	Plots of Laguerre Diagrams shaded according to the value of v_g using a random mesh of 80×40 points initialised in geostrophic space using 4.2 at (a) 6 days (b) 9 days $\Gamma = [-L, L] \times [0, H]$, where $L = 1 \times 10^6$ and $H = 1 \times 10^4$	45
5.9	Plot of Laguerre Cells generated using a random mesh of 80×40 points initialised in geostrophic space using 4.2 at (a) 0 days and (b) 2.5 days , $\Gamma = [-L, L] \times [0, H]$, where $L = 1 \times 10^6$ and $H = 1 \times 10^4$	46
5.10	Plots of Laguerre Cells generated using a random mesh of 80×40 points initialised in geostrophic space using 4.2 at (a) 6 days (b) 9 days $\Gamma = [-L, L] \times [0, H]$, where $L = 1 \times 10^6$ and $H = 1 \times 10^4$	47
5.11	Energy Error from implementation of SG/DA via Forward Euler timestepping method for 5 days	48
5.12	Energy Error from implementation of SG/DA via Heun timestepping method for 5 days	49
5.13	Energy Error from implementation of SG/DA via Forward Euler timestepping method for 10 days	49
5.14	Energy Error from implementation of SG/DA via Heun timestepping method for 10 days	50
5.15	Energy evolution for SG/DA with Euler time step scheme	50
5.16	Energy evolution for SG/DA with Heun time step scheme	51
5.17	Comparison of Energy Evolution for SG/DA with Heun/Forward Euler Time Stepping Schemes	52
5.18	Time stepping performance based on number of points initialised in the domain	53

List of Tables

5.1	Table of parameter values used in numerical implementation of SG/DA	38
5.2	Comparison of Runtime by Forward Euler and Heun's time step methods	52

Introduction

Numerical weather prediction (NWP) presents a dynamic area of research in geophysical fluid dynamics. With computer models continuing to provide longer range predictions [3] questions arise as to the limit of predictability of NWP. Whilst the mathematical theory underlying NWP has been in place as early as the 1900s, predictions were limited by the capabilities of available technology [6]. It is widely recognised that NWP models are often time-costly and memory intensive. Of course, this is not the only limitation with chaos theory and the assimilation of observed data to be considered equally [7]. The increasing impact of extreme weather events on the world population means there is a vested interest in improving the predictability of NWP.

This report is concerned with developing a numerical model for the formation of weather fronts, termed as frontogenesis. With no formal mathematical definition we follow a definition offered by Hoskins [8], where fronts are considered as regions that have length scales comparable to the height of the domain considered, whilst exhibiting large gradients in other variables in the cross direction. Frontogenesis has been studied extensively [9, 10, 11, 12, 13], naturally, as it is a significant feature of large-scale atmosphere flow (of the order 1000 km) [3]. Fronts are most canonically recognised from surface pressure diagrams in weather forecasts as seen in [?]

This process will be studied under the idealised theoretical model provided by the Semi-Geostrophic (SG) equations the governing equations which we develop in Chapter 1. Frontogenesis occurs as a result of a baroclinic instability [8], introduced in this project in the form of a vertical shear similar to the seminal work studied by Eady [14]. As discussed by Mike Cullen in [3] SG theory provides a highly predictable, general system for the study of large-scale atmospheric flow.

Work by B. Hoskins expressed the SG equations in ‘geostrophic co-ordinates’ [15]. This was subsequently developed by Shutts and Cullen [2]. In this framework the SG equations exhibit interesting geometrical properties, namely it was shown that solutions can be sought as those of an equivalent Monge-Ampère type optimal trans-

port problem [3]. This reformulation is discussed in chapter 2.

Our focus now shifts to the numerical solution of the theoretical model through optimal transport methods. Following an idea from Dr Cotter, a solution using an efficient Damped Newton Algorithm (DA) recently developed by Mèrigot et al. [16, 5, 4] is explored. In Chapter 3 we highlight the suitability of DA in solving the SG/EM equations for frontogenesis, and subsequently discuss how its implementation in building a numerical model for solving the semi-geostrophic equations is achieved in Chapter 4.

Finally, in Chapter 5 we aim to validate the suitability of this numerical algorithm in solving the semi-geostrophic equations. This will be done through suitable analysis of the error as well as a qualitative comparison to results produced by other numerical models under similar conditions [13, 17].

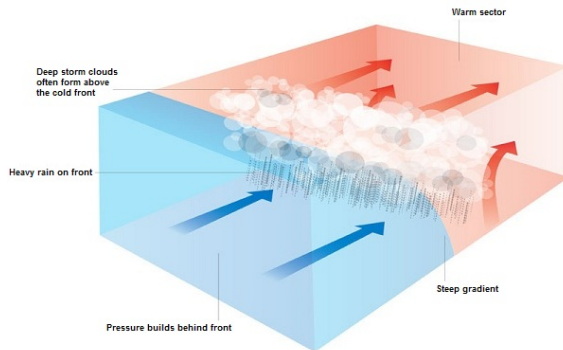


Figure 1: The mechanism behind observed cold fronts as explained by the Met Office [18]

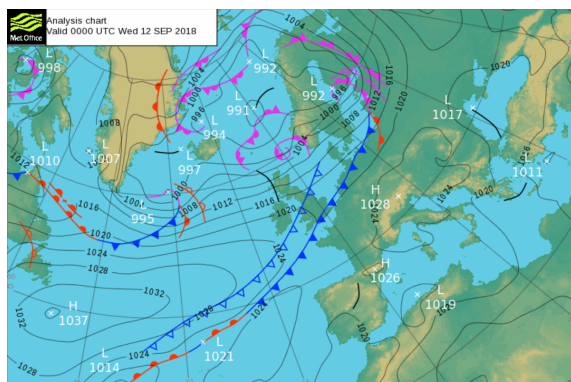


Figure 2: Surface Pressure Chart from 12/09/2018 from the Met Office website [19]

Chapter 1

The Governing Equations

The semi-geostrophic equations first introduced by Hoskins [1] based on previous work by Eliassen [20] form the basis of our model for frontogenesis. These were widely noted to provide results more frequently observed in atmospheric events than the classical quasi-geostrophic equations in their description of the formation of weather fronts [3, 1]. In this chapter a summary of key steps that lead to the Eady model for frontogenesis that was initially developed by Hoskins and Bretherton in 1972, [15]. Based on an idealised model for baroclinic instability proposed by Eady, 1949 [14], incorporating a linear stratification in density and a constant vertical shear in the horizontal velocity component. A co-ordinate transform to geostrophic co-ordinates by [1] facilitates the numerical implementation of these equations and subsequent interpretation of results. For the following the main points are summarised from [3] in formulating the model to be implemented numerically.

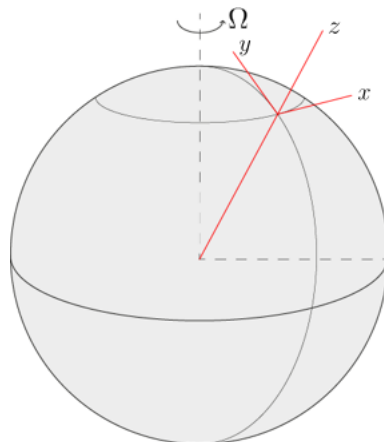


Figure 1.1: Local Cartesian co-ordinates (x, y, z) on Earth

1.1 The 3D Incompressible Boussinesq Equations

We begin with the 3D incompressible Boussinesq equations 1.1 to describe atmospheric flow. Adopting Cartesian co-ordinates (x, y, z) representing the zonal, meridional and radial directions on the Earth respectively, as shown in 1.1. A derivation of these equations can be found in [21] The corresponding velocity components are $\mathbf{u} = (u, v, w)$, with ρ_0 representing the constant density and p denoting the pressure.

$$\begin{aligned}\frac{Du}{Dt} - fv &= -\frac{1}{\rho_0} \frac{\partial p}{\partial x} \\ \frac{Dv}{Dt} + fu &= -\frac{1}{\rho_0} \frac{\partial p}{\partial y} \\ \frac{Dw}{Dt} &= -\frac{1}{\rho_0} \frac{\partial p}{\partial z} + b \\ \frac{Db}{Dt} &= 0 \\ \nabla \cdot \mathbf{u} &= 0\end{aligned}\tag{1.1}$$

Under the Boussinesq assumption that density fluctuations are small [21], the thermodynamic equation is written as the fourth equation in system 1.1. The buoyancy is characterised by Potential Temperature, θ as $b = \frac{g\theta}{\theta_0}$. By also introducing the geopotential $\phi = \frac{p}{\rho_0}$, equations 1.1 are rewritten as

$$\begin{aligned}\frac{Du}{Dt} - fv &= -\frac{\partial \phi}{\partial x} \\ \frac{Dv}{Dt} + fu &= -\frac{\partial \phi}{\partial y} \\ \frac{Dw}{Dt} &= -\frac{\partial \phi}{\partial z} + \frac{g\theta}{\theta_0} \\ \frac{D\theta}{Dt} &= 0 \\ \nabla \cdot \mathbf{u} &= 0,\end{aligned}\tag{1.2}$$

where θ_0 and g denote initial potential temperature and acceleration due to gravity respectively.

Here we have used the notation, $\frac{D}{Dt} \equiv \frac{\partial}{\partial t} + u \frac{\partial}{\partial x} + v \frac{\partial}{\partial y} + w \frac{\partial}{\partial z}$, $\nabla \equiv \left(\frac{\partial}{\partial x}, \frac{\partial}{\partial y}, \frac{\partial}{\partial z} \right)$.

Additionally if the hydrostatic approximation, that vertical acceleration is small

compared to gravity, so that, $\frac{Dw}{Dt} = 0$. Then,

$$\begin{aligned}\frac{Du}{Dt} - fv &= -\frac{\partial \phi}{\partial x} \\ \frac{Dv}{Dt} + fu &= -\frac{\partial \phi}{\partial y} \\ -\frac{\partial \phi}{\partial z} + \frac{g\theta}{\theta_0} &= 0 \\ \frac{D\theta}{Dt} &= 0 \\ \nabla \cdot \mathbf{u} &= 0.\end{aligned}\tag{1.3}$$

1.2 The Vertical Slice Model

To facilitate the study of frontogenesis a vertical slice model is introduced. This assumes that in one direction the length scale is infinite, so that variations in perturbation fields in this direction can be neglected. In this project the vertical slice considered is the $(x - z)$ plane, with the y direction considered as having infinite scale. We consider the domain, $\Gamma := [-L, L] \times [0, H]$. Perturbations to the leading-order fields are considered as functions of x, z and t only, whereas the leading order terms in θ and ϕ are functions of (y, z) . Retaining the potential temperature gradient normal to the slice is crucial to the subsequent evolution of the front. Following the ideas of Yamazaki et al. [9] we introduce,

$$\begin{aligned}\theta &= \bar{\theta}(y, z) + \theta'(x, z, t) \\ \phi &= \bar{\phi}(y, z) + \varphi(x, z, t),\end{aligned}\tag{1.4}$$

with the background field for θ chosen as

$$\bar{\theta} = -Cy,\tag{1.5}$$

where $\frac{\partial \theta}{\partial y} = -C$ is a constant, normal to the slice potential temperature gradient.

The background field for ϕ is chosen so that both background fields for θ and ϕ satisfy the third equation of 1.3,

$$-\frac{\partial \bar{\phi}}{\partial z} + \frac{g\bar{\theta}}{\theta_0} = 0,$$

with the boundary condition $\phi = 0$ at $z = H/2$. This gives,

$$\bar{\phi} = -\frac{Cgy}{\theta_0} (z - H/2).\tag{1.6}$$

To reach the final vertical slice model we substitute the forms 1.4 with expressions for the background fields 1.5 and 1.6 into equations 1.3.

$$\begin{aligned}
\frac{Du}{Dt} - fv &= -\frac{\partial}{\partial x} (\bar{\phi} + \varphi) \\
\frac{Dv}{Dt} + fu &= -\frac{\partial}{\partial y} (\bar{\phi} + \varphi) \\
0 &= \frac{\partial}{\partial z} (\bar{\phi} + \varphi) - \frac{g}{\theta_0} (\bar{\theta} + \theta') \\
0 &= \frac{\partial}{\partial t} (\bar{\theta} + \theta') + u \frac{\partial}{\partial x} (\bar{\theta} + \theta') + v \frac{\partial}{\partial y} (\bar{\theta} + \theta') + w \frac{\partial}{\partial z} (\bar{\theta} + \theta') \\
0 &= \frac{\partial u}{\partial x} + \frac{\partial v}{\partial y} + \frac{\partial w}{\partial z}
\end{aligned} \tag{1.7}$$

By neglecting $\partial/\partial y$ terms except in background variables, after rearrangement the vertical slice equations are obtained as,

$$\begin{aligned}
\frac{\partial u}{\partial t} + u \frac{\partial u}{\partial x} + w \frac{\partial u}{\partial z} - fv &= -\frac{\partial \varphi}{\partial x} \\
\frac{\partial v}{\partial t} + u \frac{\partial v}{\partial x} + w \frac{\partial v}{\partial z} + fu &= -\frac{\partial \varphi}{\partial y} + \frac{Cg}{\theta_0} (z - H/2) \\
0 &= \frac{\partial \varphi}{\partial z} - \frac{g\theta'}{\theta_0} \\
0 &= \frac{\partial \theta'}{\partial t} + u \frac{\partial \theta'}{\partial x} - Cv + w \frac{\partial \theta'}{\partial z} \\
0 &= \frac{\partial u}{\partial x} + \frac{\partial w}{\partial z}
\end{aligned} \tag{1.8}$$

We redefine the material derivative operator as $\frac{D}{Dt} \equiv \frac{\partial}{\partial t} + u \frac{\partial}{\partial x} + w \frac{\partial}{\partial z}$, and gradient operator $\nabla = (\frac{\partial}{\partial x}, \frac{\partial}{\partial z})$ so that,

$$\begin{aligned}
\frac{Du}{Dt} - fv &= -\frac{\partial \varphi}{\partial x} \\
\frac{Dv}{Dt} + fu - \frac{Cg}{\theta_0} (z - H/2) &= -\frac{\partial \varphi}{\partial y} \\
\frac{\partial \varphi}{\partial z} - \frac{g\theta'}{\theta_0} &= 0 \\
\frac{D\theta'}{Dt} - Cv &= 0 \\
\nabla \cdot \mathbf{u} &= 0.
\end{aligned} \tag{1.9}$$

1.3 The Geostrophic Momentum Approximation

To reach the final semi-geostrophic Eady model for frontogenesis the Geostrophic Momentum approximation is made. Developed by Hoskins, 1975 [1], where further

detail can be found, the following section gives a brief summary of the key arguments.

Going back to equations 1.2. We consider an expansion in the Rossby number $\epsilon = U/fL$ where U and L are horizontal velocity and length scaled respectively. Expanding the momentum equations in 1.9 in leading-order (geostrophic) and first order (ageostrophic) terms in ϵ , so that,

$$\mathbf{u} = \mathbf{u}_g + \epsilon \mathbf{u}_a \quad \varphi = \varphi + \epsilon \varphi_a$$

Acceleration terms are found to be $O(\epsilon)$ so that at the leading order the geostrophic balance is found to be,

$$fv_g = -\frac{\partial \varphi}{\partial x} \quad -fu_g = -\frac{\partial \varphi}{\partial y} \quad (1.10)$$

Subsequent expansion in the Rossby number as detailed in Hoskins 1975, [1] finds the prognostic equations for ageostrophic variables to be as in 1.11, adapted for the vertical slice model as,

$$\begin{aligned} \frac{Du_g}{Dt} - fv + \frac{\partial \varphi}{\partial x} &= 0, \\ \frac{Dv_g}{Dt} + fu - \frac{Cg}{\theta_0} (z - H/2) &= 0, \\ \frac{D\theta'}{Dt} - Cv_g &= 0, \\ \frac{\partial \varphi}{\partial z} - g \frac{\theta'}{\theta_0} &= 0, \\ \nabla \cdot \mathbf{u} &= 0. \end{aligned} \quad (1.11)$$

We now use a scaling argument to show that in the first of equations 1.11 we can neglect the $\frac{Du_g}{Dt}$ term. This comes from noting that using the typical scaling scale T for time we see that the scaling for φ from the geostrophic balance gives,

$$fU = \frac{[\varphi]}{L} \implies [\varphi] = fUL$$

So that the scalings in the first equation of 1.11 are,

$$\left[\frac{Du_g}{Dt} \right] = \frac{U}{T} = fU\epsilon, \quad [fv_g] = fU, \quad \left[\frac{\partial \varphi}{\partial z} \right] = fU$$

Where we have used $U/T = \frac{U}{L/U} = fU\epsilon$. From this we see that the first term is $O(\epsilon)$ so that it can be neglected as the Rossby number is small. This gives the final

set of equations as,

$$\begin{aligned}
-fv_g + \frac{\partial \varphi}{\partial x} &= 0, \\
\frac{Dv_g}{Dt} + fu - \frac{Cg}{\theta_0}(z - H/2) &= 0, \\
\frac{D\theta'}{Dt} - Cv_g &= 0, \\
\frac{\partial \varphi}{\partial z} - g \frac{\theta'}{\theta_0} &= 0, \\
\nabla \cdot \mathbf{u} &= 0.
\end{aligned} \tag{1.12}$$

Physically the reason for retaining $\frac{Dv_g}{Dt}$ is that this represents a fast flow in the direction of the front where as $\frac{Du}{Dt}$ is neglected as it is lot smaller in comparison to the rest of the term.

A detailed derivation of the corresponding energy integral can be found in [3]. Here we restate it,

$$E = \iint_{\Gamma} \frac{1}{2} v_g^2 - \frac{g\theta'}{\theta_0} (z - H/2) dx dz. \tag{1.13}$$

Equations 1.12 form the basis of the subsequent investigation of frontogenesis in this report. They are to be solved over the domain $\Gamma = [-L, L] \times [0, H]$, with the periodic boundary conditions in x and the rigid-lid boundary condition $w = 0$ on $z = 0, H$. Note that in these equations the velocity u, w appears implicitly in the material derivative.

The key mechanism contributing to front formation seen later in this project (see Chapter 5) is a consequence of a baroclinic instability introduced by Cullen 2006 [3] in the form of a perturbation to θ' ,

$$\theta' = \frac{N^2 \theta_0 z}{g} + B \sin(\pi(x/L + z/H)). \tag{1.14}$$

The Brunt-Väisälä frequency $N^2 = \frac{g}{\theta_0} \frac{\partial \theta}{\partial z}$ characterises the stratification of density in the slice. The instability in the second term of 1.14 is a of the normal mode form.

Aside: It is worth noting that Eady's original model for baroclinic instability was developed under a quasi-geostrophic model, where $\epsilon = Fr \ll 1$ in contrast semi-geostrophic theory the assumes, $\epsilon \ll 1$ with $\epsilon < Fr$. Whilst we refer to the 'Eady Model' in fact this model is very different to that proposed by Eady [14]. The main similarity, and key assumption in Eady's work is the investigation of baroclinic instability in the presence of a background shear flow.

Chapter 2

The Frontogenesis Model as an Optimal Transport Problem

The semi-geostrophic equations have previously been rigorously analysed [1, 22, 17] and models subsequently developed to include momentum diffusion [23, 13]. The existence of smooth solutions for the Eady Model for frontogenesis 1.12 is shown in [24]. Perhaps one of the most exciting developments in the study of frontogenesis was the reformulation of the semi-geostrophic equations into a Monge-Ampère equation for mass transportation [25] **Comment: CHECK!**. It is shown in [3] that through a transformation to geostrophic co-ordinates as described in section 1.3 the energy integral can be viewed as the 'cost' in a mass transportation problem. This reformulation has allowed a deeper insight into the behaviour of the equations through numerical solutions developed from methods in computational geometry. In this chapter the arguments given in [3] are summarised to highlight the application of optimal transport theory to the Eady Model for frontogenesis 1.12. **Comment: smooth solutions only in geostrophic co-ordinates**

2.1 The Semi-Geostrophic Equations

To facilitate the implementation of the numerical scheme we will subsequently use to solve equations 1.12 we transform to geostrophic co-ordinate system first introduced by Hoskins [1] in the horizontal directions (x, y) . The geostrophic co-ordinates describe the position of particles had they evolved under their geostrophic velocity. This transformation was later developed by Cullen [3] to include a transformation in terms of θ' in the vertical direction. The geostrophic transformation $\Phi : (x, z) \rightarrow (X, Z)$

$$X = x + \frac{v_g}{f}, \quad Z = \frac{g\theta'}{f^2\theta_0} \quad (2.1)$$

By defining

$$P = \frac{1}{2}x^2 + \frac{1}{f^2}\varphi \quad (2.2)$$

It is clear that,

$$\nabla P = \left(x + \frac{1}{f^2} \frac{\partial \varphi}{\partial x}, \frac{1}{f^2} \frac{\partial \theta'}{\partial z} \right) = \left(x + \frac{v_g}{f}, \frac{g\theta'}{f^2\theta_0} \right)$$

So that upon substitution from the first and fourth equations in 1.12 we find,

$$\nabla P = (X, Z) \quad (2.3)$$

By noting that,

$$\frac{DX}{Dt} = \frac{Dx}{Dt} + \frac{1}{f} \frac{Dv_g}{Dt} = u + \frac{1}{f} \frac{Dv_g}{Dt}, \quad \frac{DZ}{Dt} = \frac{g}{f^2\theta_0} \frac{D\theta'}{Dt}$$

the momentum equations from 1.12 are transformed into geostrophic co-ordinates as

$$\frac{DX}{Dt} - \frac{Cg}{f\theta_0} (z - H/2) = 0, \quad \frac{DZ}{Dt} - \frac{Cg}{f\theta_0} (X - x) = 0, \quad (2.4)$$

It is also shown in [3] that the continuity equation holds in geostrophic co-ordinates. with $\mathbf{U} = \frac{Cg}{f\theta_0} (z - H/2, X - x)$ Putting together equations 2.2, 2.3, 2.4 the Eady Model in geostrophic co-ordinates is

$$\begin{aligned} \frac{DX}{Dt} - \frac{Cg}{f\theta_0} (z - H/2) &= 0 \\ \frac{DZ}{Dt} - \frac{Cg}{f\theta_0} (X - x) &= 0, \\ P &= \frac{1}{2}x^2 + \frac{1}{f^2}\varphi, \end{aligned} \quad (2.5)$$

$$\nabla P = (X, Z)$$

$$\nabla \cdot \mathbf{U} = 0$$

The corresponding energy integral given by transforming the Energy 2.6 with 2.1 is,

$$E = f^2 \iint \frac{1}{2} (X - x)^2 - Z (z - H/2) dx dz \quad (2.6)$$

Equations 2.5 with 2.6 are termed by Hoskins as the semi-geostrophic equations[1]. Hereafter we will refer to the system of equations 2.5 with 1.14 as SG/EM, denoting the Eady model for baroclinic instability in the semi-geostrophic equations.

2.2 Energy Minimisation as an Optimal Transportation Problem

It is shown in [3] and references therein that the semi-geostrophic equations in the form 2.5 can be characterised as an energy minimisation problem. In this section we follow the work of Cullen [3] in carrying out this reformulation and develop it to take the form of an optimal transport problem with a quadratic cost function as in [5]. This amounts to the solution of 2.5 as finding (X, Z) which minimise the energy and subsequently finding their time evolution using 2.5.

2.2.1 Finding an Inverse Transformation

Consider an initial set of points in geostrophic space (X, Z) . To find the trajectory of points in geostrophic space and consequently to solve 2.5 requires the corresponding values $(x(X, Z), z(X, Z))$. This requires the existence of a unique inverse to the transform 2.1. Following [3], the function $R(X, Z)$ is defined as,

$$R(X, Z) = x(X, Z)X + z(X, Z)Z - P(x, y, z)$$

To rewrite the energy integral 2.6 in geostrophic co-ordinates requires the Jacobian of the inverse transformation $\Phi^{-1} : (X, Z) \rightarrow (x, z)$,

$$\sigma(X, Z) = \frac{\partial x}{\partial X} \frac{\partial z}{\partial Z} - \frac{\partial z}{\partial X} \frac{\partial x}{\partial Z} \quad (2.7)$$

Noting that,

$$\frac{\partial R}{\partial X} = x + X \frac{\partial x}{\partial X} + Z \frac{\partial z}{\partial X} - \frac{\partial P}{\partial x} \frac{\partial x}{\partial X} - \frac{\partial P}{\partial x} \frac{\partial z}{\partial X}$$

Similarly,

$$\frac{\partial R}{\partial Z} = X \frac{\partial x}{\partial Z} + z + Z \frac{\partial z}{\partial Z} - \frac{\partial P}{\partial Z} \frac{\partial x}{\partial Z} - \frac{\partial P}{\partial Z} \frac{\partial z}{\partial Z}$$

Using $\nabla P = (X, Z)$, we find,

$$\nabla_{(X, Z)} R = \left(\frac{\partial R}{\partial X}, \frac{\partial R}{\partial Z} \right) = (x, z) \quad (2.8)$$

This is convenient as it allows us to rewrite 2.7 as,

$$\sigma(X, Z) = \frac{\partial^2 R}{\partial X^2} \frac{\partial^2 R}{\partial Z^2} - \frac{\partial^2 R}{\partial X \partial Z} \frac{\partial^2 R}{\partial Z \partial X} = \det(\text{Hess } R) \quad (2.9)$$

As stated in [3] this is a form of the classical **Monge Ampère equation** for a given $\sigma(X, Z)$. Paired with the boundary condition that the fluid in physical co-ordinates

stays within the domain, Γ , (ie) $(x, z) = \nabla_{(X, Z)} R \in \Gamma$. This can be expressed as,

$$\iint_{\mathbb{R}^2} \sigma(X, Z) dXdZ = \iint_{\Gamma} dx dz \quad (2.10)$$

Physically this is equivalent to conservation of volume for all time so that σ satisfies a continuity equation,

$$\frac{D_{(X, Z)} \sigma}{Dt} = \frac{\partial \sigma}{\partial t} + \frac{\partial U}{\partial X} \frac{\partial \sigma}{\partial X} + \frac{\partial W}{\partial Z} \frac{\partial \sigma}{\partial Z} \quad (2.11)$$

This gives a prognostic equation for $\sigma(X, Z)$. Together with equations 2.9, 2.8 and the constraint 2.10 which allow an inverse transformation to be found the inverse transformation. Arguments in [3] show that if P is a convex function then $R(X, Z)$ is a convex function, this in turn gives us that X, Z are monotone functions of x, z respectively and similarly x, z are monotone functions of X, Z . This gives uniqueness of the inverse transformation, making these arguments justified. Further details can be found in [3]

2.2.2 The Monge-Ampère equation and Optimal Transportation

Again giving an overview of the arguments in [3] we show how the Monge-Ampère equation 2.9 can be solved as an optimal transport problem.

The density σ can be seen to define a measure on \mathbb{R}^2 , where the measure of the set $A \subseteq \mathbb{R}^2$ is defined as $\nu(A) = \iint_A \sigma(X, Z) dXdZ$. On the domain Γ in physical coordinates (x, z) we consider the scaled Lebesgue measure $\mu(\gamma) = \text{Area}(\Gamma)^{-1} \iint_{\gamma} dx dz$, where $\gamma \subseteq \Gamma$ and $\text{Area}(\Gamma) = \iint_{\Gamma} dx dz$. Note this defines a probability measure on Γ . Considering mappings $s : \mathbb{R}^2 \rightarrow \Gamma$ that preserve measure so that if $\gamma = s(A)$, we have $\nu(A) = \mu(\gamma)$. The reader is referred to [26] for a rigorous explanation of concepts in measure theory.

With this in mind, given the mapping $s : \mathbb{R}^2 \rightarrow \Gamma$ the energy is defined in [3] as the following,

$$E = f^2 \iint \frac{1}{2} (X - \tilde{x})^2 - Z (\tilde{z} - H/2) \sigma dXdZ \quad (2.12)$$

where $(\tilde{x}, \tilde{z}) = s(X, Z)$. The solution for equations 2.5 is then encapsulated in Theorem (3.4) of [3] which says that the condition for the energy to be minimised

is that,

$$s(X, Z) = \nabla R \quad (2.13)$$

with condition 2.10 as above.

We now put this into the context of the discrete problem which will be subsequently solved in the implementation of the optimal transport solver from [16]. In this case we consider Γ to be a partition into N ‘fluid parcels’ of equal volume. For convenience we consider the case where the total volume of Γ is $\iint_{\Gamma} dxdz = 1$.

The density σ is defined discretely for N points $\mathbf{Y}_i = (X_i, Z_i)$ in geostrophic space as $\sigma(X, Y) = \sum_{i=1}^N \frac{1}{N} \delta(\mathbf{Y} - \mathbf{Y}_i)$. Note, this also gives $\iint_{\mathbb{R}^2} \sigma(X, Z) dXdZ = 1$. The problem in this case becomes finding a map $s : \mathbb{R}^2 \rightarrow \Gamma$ such that the energy,

$$E = f^2 \iint \frac{1}{2} (X_i - \tilde{x})^2 - Z_i (\tilde{z} - H/2) \sigma \, dXdZ \quad (2.14)$$

is minimised and such that the volume of the associated fluid ‘parcels’, (ie) the sets $A_i = s^{-1}(X_i, Z_i)$ is preserved. Figure 2.1 illustrates such a transformation. Theorem (3.11) from [3] proves the existence of such a map for the density σ . The final piece

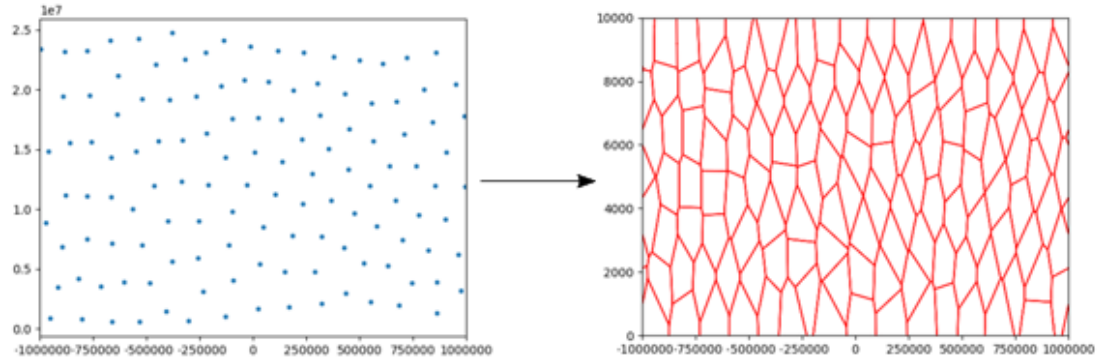


Figure 2.1: Figure illustrating a map from geostrophic points to fluid ‘parcels’ that preserves volume.

in the formulation of the solution of the semi-geostrophic equations as an optimal transport problem uses Theorem (3.16) from [3]. We restate this using the notation from this report.

Theorem 2.2.1. *Given probability measures σ, μ with bounded supports $\Sigma \subset \mathbb{R}^2$, $\Gamma \subset \mathbb{R}^2$. There exist optimal maps $t : \Sigma \rightarrow \Gamma$ and $t^{-1} : \Gamma \rightarrow \Sigma$ which are inverses and minimise a quadratic cost function given by*

$$\iint_{\mathbb{R}^2} \left(\frac{1}{2} f^2 |\mathbf{Y} - t(\mathbf{Y})|^2 \right) \sigma \, dXdZ$$

Furthermore, these maps are unique up to sets of measure zero.

The reader is referred to [26] for a detailed discussion of measure theory and zero measure sets. The proof 2.2.1 is given in [3] and is a culmination of the results stated above. Γ is clearly a bounded domain by definition and Σ is a set of finite points, so it too is also bounded. Furthermore, since σ and μ are defined so that their integrals over Σ and Γ are unity, they are probability measures over their respective domains.

It remains to show that the minimisation of the quadratic cost function is equivalent to minimising the energy. For this we transform the cost function to physical co-ordinates as,

$$\iint_{\mathbb{R}^2} \left(\frac{1}{2} f^2 |t^{-1}(\mathbf{y}) - \mathbf{y}|^2 \right) dx dz.$$

The following Lemma proves this to be equivalent to minimising the energy given by 2.6.

Lemma 2.2.2. *Minimising the Energy integral given by,*

$$E = f^2 \iint_{\Gamma} \frac{1}{2} (X - x)^2 - Z(z - H/2) dx dz$$

is equivalent to minimising the quadratic cost integral given by,

$$E = f^2 \iint_{\Gamma} \frac{1}{2} ((X - x)^2 + (Z - z)^2) dx dz$$

Proof. We begin by noting that the difference in the energy integrals is in the potential energy term, so it suffices to show that the minimisation of these terms is equivalent. Expanding to see,

$$\iint_{\Gamma} -Z(z - H/2) dx dz = \iint_{\Gamma} -Zz + \frac{ZH}{2} dx dz \quad (2.15)$$

$$\iint_{\Gamma} \frac{1}{2} (Z - z)^2 dx dz = \iint_{\Gamma} \frac{1}{2} Z^2 - Zz + \frac{1}{2} z^2 dx dz \quad (2.16)$$

Recalling that Z is a function of (x, z) , the treatment of terms with this variable need to be considered carefully. As both 2.15 and 2.16 contain $\iint_{\Gamma} -Zz$, this can also be omitted from consideration.

Considering $\iint_{\Gamma} \frac{1}{2} Z^2 dx dz$. Given a partition of Γ into N subsets, up to zero measure sets, so that $\Gamma = \bigcup_{i=1}^N c_i$. Applying the transform $\Phi : (x, z) \rightarrow (X, Z)$, and using

that the transform maps subsets in physical space to points in geostrophic space

$$\sum_{i=1}^N \iint_{c_i} \frac{1}{2} Z^2 dx dz = \sum_{i=1}^N \iint_{\Phi(c_i)} \frac{1}{2} Z^2 \sigma(X, Z) dX dZ$$

But since $\sigma(X, Z) = \sum_{i=1}^N \frac{1}{N} \delta(\mathbf{Y} - \mathbf{Y}_i)$

$$\implies \sum_{i=1}^N \frac{1}{N} \frac{1}{2} Z_i^2$$

However this is a fixed value. Similar arguments give that,

$$\sum_{i=1}^N \iint_{c_i} \frac{HZ}{2} dx dz = \sum_{i=1}^N \frac{HZ_i}{2}$$

Hence, the minimisation of 2.15 and 2.16 is equivalent. \square

To summarise the results of this Chapter, we began by transforming the semi-geostrophic equations to geostrophic co-ordinates. In this setting finding the solution to equations 2.5 was shown to amount to an energy minimisation problem with the energy being defined by 2.6. Through the use of the Jacobian for the transformation $\sigma(X, Z)$ and an appropriately defined function $R(X, Z)$ we were able to show this energy minimisation to be the solution of a Monge-Ampère equation. Subsequently, through the use of probability measures this was shown to be equivalent to a discrete optimal transport problem with quadratic cost. Finally by proving the equivalence of minimising energy to minimising the quadratic cost function the problem is formulated as an optimal transport problem.

Chapter 3

Using Semi-discrete Optimal Transport to solve the Semi-Geostrophic Equations

The Damped Newton algorithm, hereafter DA, developed by Mérigot et al. [16] solves a semi-discrete Monge-Ampère type optimal transport problem. It's efficiency (linear convergence) [4] make it practical for implementation in the solution for equations 2.5. Further detail describing the application of the algorithm in the solution to the Eady Model is given in chapter 4. In this chapter an overview of semi-discrete optimal transport is given using definitions given in [4, 16] its application to the energy minimisation problem described in 2.

3.1 Semi-discrete Optimal Transport

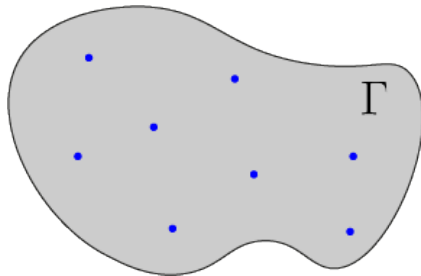


Figure 3.1: A discrete (target) set $Y \subseteq \mathbb{R}^2$ represented by blue points in a compact domain (source) $\Gamma \subseteq \mathbb{R}^2$

Optimal transport problems describe the problem of finding a map between two sets, a target set and a source set, each with an associated density, in such a way that the ‘cost’associated with the mapping is minimised. In semi-discrete optimal transport the target set is a finite set.

In Kitagawa et al. [4] a wonderful analogy with travel distance to bakeries in a city is made, where the source density is considered as the distribution of population in a city and the discrete target set is the locations of bakeries in the city. The cost to be minimised is travel distance to the bakeries.

In this report the problem will be explained in the context in which it will subsequently be implemented. Namely, the source set is the domain Γ , the physical space described in section 2 and the target set, the set of points in geostrophic space. The optimal transport problem finds a partition of the domain, up to sets of measure zero, such that every point in a region of the partition is closest to the point at the centre of that region. In this analogy the cost being minimised is the travel distance to the point \mathbf{Y}_i , $c(\mathbf{x}, \mathbf{Y}_i) = \|\mathbf{x} - \mathbf{Y}_i\|^2$, where $\mathbf{x} \in \Gamma$. This is illustrated in figure 3.2 below

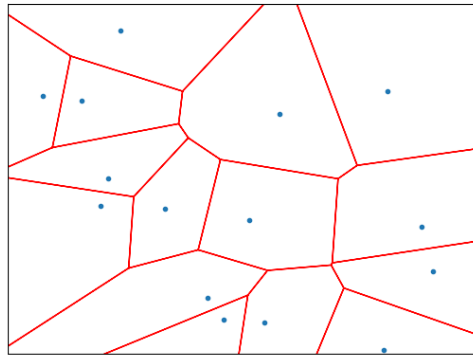


Figure 3.2: The image showing how a domain would be divided into areas based on minimising distance to the blue points. This is a Voronoi tessellation of the domain Γ based on the minimisation of $c(\mathbf{x}, \mathbf{Y}_i)$

To put this into a more rigorous mathematical setting, given a domain $\Gamma \subseteq \mathbb{R}^2$ and discrete set of N points $Y = \{\mathbf{Y}_i = (X_i, Z_i), \quad 1 \leq i \leq N\} \subset \mathbb{R}^2$,

Definition 3.1.1. Source measure

Defined on the domain Γ . $\mu(A) = \text{Area}(\Gamma)^{-1} \int_A dx dz$, $A \subseteq \Gamma$. Note this defines a probability measure with a uniform probability density on Γ .

Definition 3.1.2. Target measure

Defined on \mathbb{R}^2 $\nu(X, Z) = \sum_{i=1}^N \sigma_i \delta(\mathbf{Y} - \mathbf{Y}_i)$, with finite support on \mathbb{R}^2 . Note this defines a discrete probability measure when $\nu(\mathbb{R}^2) = 1$, for appropriate choice of σ_i .

Definition 3.1.3. Voronoi Cells

The regions enclosed by the red lines and boundaries of the domain in 3.2 are defined

as Voronoi cells, $\text{Vor}(\mathbf{Y}_i) := \{\mathbf{x} \in \Gamma \text{ st } \forall Y_j \in Y \ c(\mathbf{x}, \mathbf{Y}_i) \leq c(\mathbf{x}, \mathbf{Y}_j)\}$. The diagram is referred to as a Voronoi tesselation.

Definition 3.1.4. Transport map

$T : \Gamma \rightarrow Y$ between the source measure μ and the target measure on Y , μ if $T_{\#}\mu = \nu$.

Definition 3.1.5. Pushforward of a measure μ by a map $T : \Gamma \rightarrow Y$ is $T_{\#}\mu = \sum_{\mathbf{Y}_i \in Y} \mu(T^{-1}(\mathbf{Y}_i)) \delta(\mathbf{Y} - \mathbf{Y}_i)$, the sum of the measures of the sets mapped to the points \mathbf{Y}_i under T

From these definitions we can see that the optimal transport map is given by,

$$T(\mathbf{x}) = \arg \min_{\mathbf{Y}_i \in Y} (c(\mathbf{x}, \mathbf{Y}_i)) \iff \nu(\mathbf{Y}_i) = \mu(\text{Vor}(\mathbf{Y}_i)) \quad (3.1)$$

3.2 Laguerre Cells and the Inclusion of weights

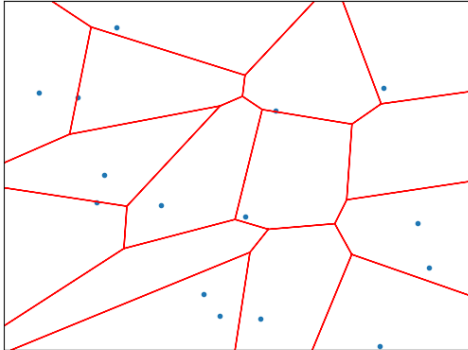


Figure 3.3: Given a uniform source and target density the Laguerre diagram produced by finding weights using DA for optimal transport

Considering again figure 3.2 it is clear that if the density across the domain Γ is uniform the distribution of area corresponding to each bakery is certainly not. For example, the Voronoi cells at the top right of the diagram in figure 3.2 are much larger in area than those in the centre of the diagram. This raises the problem of finding a way to create a partition such that each cell has the same area. This is done by introducing an additional “weight” argument to the cost. We denote the weights by $\psi_i = \psi(\mathbf{Y}_i) \in \mathbb{R}$. In the case of the bakeries the weights might represent the price of bread at a specific bakery. For this we introduce the notion of Laguerre cells.

Definition 3.2.1. Laguerre Cells

The regions enclosed by the red lines and boundaries of the domain in figure 3.3,
 $\text{Lag}_{\mathbf{Y}_i}(\psi) := \{\mathbf{x} \in \Gamma \text{ st } \forall \mathbf{Y}_j \in Y \text{ } c(\mathbf{x}, \mathbf{Y}_i) + \psi(\mathbf{Y}_i) \leq c(\mathbf{x}, \mathbf{Y}_j) + \psi(\mathbf{Y}_j)\}$

In this case, the optimal transport map is given by

$$T_\psi : x \rightarrow \operatorname{argmin}_i \|x - y_i\|^2 + \psi_i, \text{ where } \psi_i \text{ is a family of weights on } Y [16].$$

The problem is then finding the weights ψ_i associated to the points \mathbf{Y}_i such that $\mu(\text{Lag}_{\mathbf{Y}_i}(\psi)) = \nu(\mathbf{Y}_i) = \sigma_i$. The Damped Newton's Algorithm from Mérigot, Meyron and Thibert (2017) [16] finds such ψ_i .

Supposing that both the source density and target density are uniform, (ie) in definition 3.1.2 the Laguerre cells as found by DA developed in [16] are shown in figure 3.3. The Laguerre diagram highlights the fact that the densities are both specified to be uniform probability densities. In figure 3.2 the target density was not specified. This means that points are not necessarily interior to their corresponding Laguerre cells, however the cells have equal area. The cells in this case are the Laguerre cells defined above, and the weights that define the optimal transport map was found by [16] as

$$T(x) = \arg \min_{\mathbf{Y}_i \in Y} (c(\mathbf{x}, \mathbf{Y}_i) + \psi_i)$$

For the remainder of this report we will consider cases where both the source density and target density are uniform and the quadratic cost function is,

$$c(\mathbf{x}, \mathbf{Y}_i) = \|\mathbf{x} - \mathbf{Y}_i\|^2$$

3.3 Applying semi-discrete optimal transport to solving the semi-geostrophic equations

As shown in [3] equations 1.12 can be recast as an optimal transport problem using the transformation to geostrophic co-ordinates introduced by Hoskins [1]. In this section we outline how DA is applied to equations 1.12.

The optimal transport problem considered in the frontogenesis problem is the minimisation of the energy, restated from equation 2.6

$$E = f^2 \iint \frac{1}{2} (X - x)^2 - Z (z - H/2) \, dx \, dz \quad (3.2)$$

as shown by Lemma 2.2.2 this is equivalent to minimising 2.2.2,

$$E = \frac{f^2}{2} \iint ((X - x)^2 + (Z - z)^2) \, dx \, dz \quad (3.3)$$

Considering the geostrophic co-ordinates as the target set of finite set of points for the optimal transport problem from the domain $\Gamma = [-L, L] \times [0, H]$. The DA Algorithm finds the weights such that the area of each Laguerre cell is preserved. Physically, this amounts to the condition that the volume is conserved.

3.4 Extension for Periodic Boundary Conditions

As stated in Chapter 1 in the model for frontogenesis boundary conditions consider periodicity in x . This must be accounted for in the implementation of the Damped Newton Algorithm. A significant proportion of work in developing an accurate algorithm for SG/EM was to implement the functions in DA to correctly treat the periodic boundary conditions.

This inclusion of periodic boundary conditions allows Laguerre cells to cover areas over the right and left boundaries. This means that the Laguerre edges must be continuous across the boundaries if copies of the Laguerre diagram were placed on each boundary. This is illustrated in figure 3.5. The Laguerre cells must have the same mass, for example, in figure 3.4 below the top right cell extends to the left of the domain. The sum of the areas of each component of the cell must be the same as a cell in the centre of the diagram. The area of each cell remains the same as in 3.3 however the boundaries of the Laguerre cells are continuous across the left and right boundaries of the domain.

3.4.1 Calculating Moments of a cell with Periodic Boundary Conditions

In applying the time stepping of for solving 2.5 we will require the moments of the Laguerre cells specifically to calculate the mass and centroids of the cells. Again this requires an extension for periodic boundary conditions as we see in figure 3.4 the area of the cell is split in the domain. Again this is treated by making copies of the points to the right $-2L$ and left $+2L$ of the domain, as seen in figure 3.5. The moments of cells when the density isn't periodic for the Laguerre cell C_n of point n are given by,

O^{th} Moment

$$M_0 = \int_{C_n} dx \, dz \quad (3.4)$$

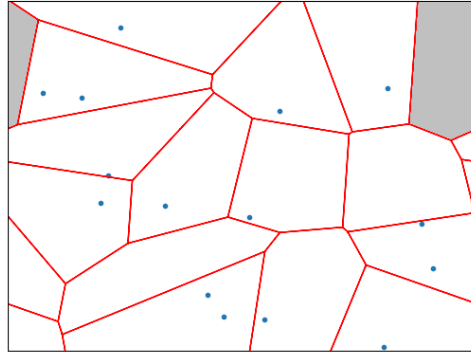


Figure 3.4: The solution to the optimal transport of the same points shown in figure 3.3, however with the density initialised with periodic boundary conditions in x . The area shaded in grey represents a single Laguerre cell.

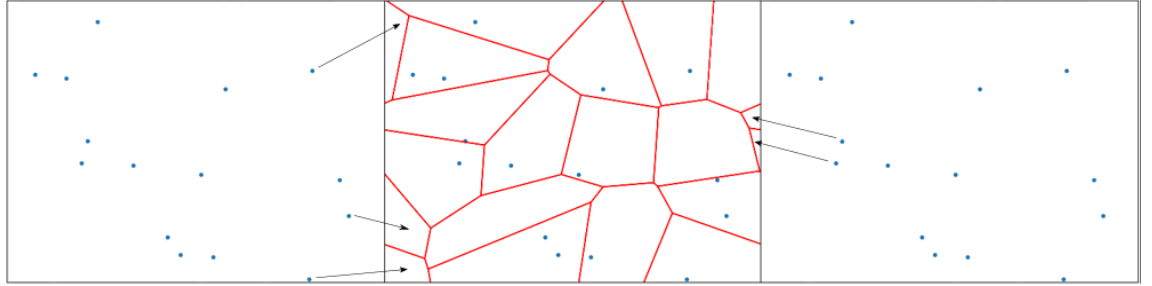


Figure 3.5: The image above shows how the Laguerre diagram for periodic boundary conditions is created with 'ghost' points on either side of the domain. Arrows show where ghost points contribute to Laguerre cells with positive mass in the domain $\Gamma = [-L, L] \times [0, H]$ **Comment: more labelling of domains**

1st Moment

$$M_{1x} = \int_{C_n} x \, dx dz, \quad M_{1z} = \int_{C_n} z \, dx dz \quad (3.5)$$

2nd Moment

$$M_{2x} = \int_{C_n} x^2 \, dx dz, \quad M_{2z} = \int_{C_n} z^2 \, dx dz, \quad M_{2xz} = \int_{C_n} xz \, dx dz \quad (3.6)$$

To extend this for periodic boundaries we sum the contribution to the moment for each copy of the point separately and sum the results. For example in the case of mass where the points n, n_{-2L}, n_{2L} represent the points in the domain $\Gamma, \Gamma - 2L, \Gamma + 2L$ respectively the mass of the cell is given by,

$$M_0 = \int_{C_n} dx dz + \int_{C_{n-2L}} dx dz + \int_{C_{n+2L}} dx dz \quad (3.7)$$

Note for each point only two of the quantities in the sum above will return a value greater than zero. The first and second moments are found similarly.

3.4.2 Mapping to the Fundamental Domain

Under the geostrophic transformation 2.1 and also in time-stepping points in geostrophic space it is possible for points to travel exterior the boundaries of the domain Γ . In the x direction the boundary conditions imposed are periodic. If points are mapped so that their x -co-ordinates are exterior to the interval $[-L, L]$, they can be mapped to the domain Γ , the ‘fundamental domain’, using the periodicity, without affecting the result. **Comment: better phrasing please** In fact, in the implementation of DA this is necessary at every time step to ensure that the mass of cells remains positive. This is implemented by the function ‘to_fundamental_domain’ adapted from DA [5] to treat periodic boundary conditions in x . An example of this is shown in figure 3.6 below, where the fundamental domain being considered is $[0, 1] \times [0, 1]$.

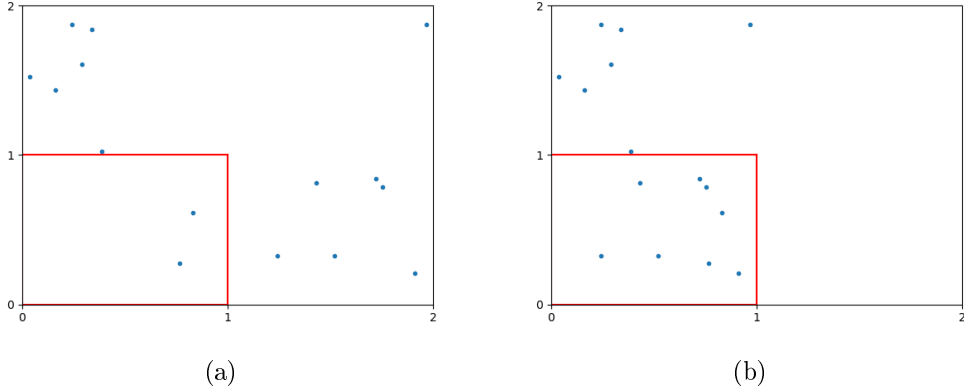


Figure 3.6: Plots of a random set of points initialised in $[0, 2] \times [0, 2]$ before (a) and after (b) being mapped to the fundamental domain $[0, 1] \times [0, 1]$

To explain this rigorously, we consider the domain described by $[x_0, y_0] \times [x_1, y_1]$. Since we are only considering periodic boundary conditions in x , only the x co-ordinates will be mapped.

The mapping is performed by first finding the distance of the point from the left boundary of the domain as a ratio of the width of the domain. This is then added to left bound to give a value for x , \tilde{x} that is in the fundamental domain.

$$X = x - \left\lfloor \frac{x - x_0}{x_1 - x_0} \right\rfloor$$

$$\tilde{x} = x_0 + (x_1 - x_0)X$$

This is implemented as: **Comment: insert to _fundamental_domain code**

3.5 Validating the application of DA to the system SG/EM

In the sections above we have described how the system of equations SG/EM can be reformulated as an optimal transport problem and how the target set of points in geostrophic space can be discretised by the use of Dirac masses to define a probability density. Defining a continuous uniform density on the domain Γ we see that finding a transport map which takes geostrophic points to areas in the physical domain whilst minimising the energy 2.2.2 is an optimal transport problem.

In this chapter the application of DA to solving semi-discrete optimal transport through the use of Laguerre cells in [16, 4] was described. By viewing the source density as a tesselation of fluid ‘parcels’. Viewed as Laguerre cells the transport of geostrophic points to fluid parcels in the physical domain minimising a quadratic cost function is a form of semi-discrete optimal transport problem solved by DA. We showed by lemma 2.2.2 that minimising the energy was equivalent to minimising a quadratic cost function.

In Kitawaga et al. [4] and Mérigot el al. [16] showed that the algorithm DA exhibits global linear convergence, which is much better than other algorithms for semi-discrete optimal transport where convergence is typically $O\left(\frac{N^3}{\epsilon}\right)$ where N is the number of points in the discrete target set and ϵ is the desired error [4]. In fact in their own experiments the algorithm exhibited even better convergence than this!

Comment: Sparsity?? Such an efficient algorithm is particularly attractive for solving SG/EM as the optimal transport problem will need to be solved at each time step for the set of geostrophic points generated.

Chapter 4

A Numerical Solution to the Eady Model for Frontogenesis

In this section the numerical implementation including the use of the Damped Newton Algorithm developed by [16] is explained in detail. Restating the problem, we are solving the semi-geostrophic equations 1.12 over the domain $\Gamma := [-L, L] \times [0, H]$.

$$\begin{aligned} -fv_g + \frac{\partial \varphi}{\partial x} &= 0, \\ \frac{Dv_g}{Dt} + fu - \frac{Cg}{\theta_0} (z - H/2) &= 0, \\ \frac{D\theta'}{Dt} - Cv_g &= 0, \\ \frac{\partial \varphi}{\partial z} - g \frac{\theta'}{\theta_0} &= 0, \\ \nabla \cdot \mathbf{u} &= 0. \end{aligned}$$

With boundary conditions:

- Rigid lid condition $w = 0$ on $z = 0, H$
- Periodic boundary conditions in x

Together with a baroclinic instability described by 1.14 as

$$\theta' = \frac{N^2 \theta_0 z}{g} + B \sin(\pi(x/L + z/H)) \quad (4.1)$$

The steps involved in solving the Eady Model for frontogenesis described above are detailed below,

4.1 Algorithm for solving the semi-geostrophic Eady model for Frontogenesis

Step 1 Initialise a set of $2N^2$ random points in physical space, or $\Delta x = \frac{L}{N}$ and $\Delta z = \frac{H}{N}$ for a regular grid.

Step 2 Transform physical points to Geostrophic space using the co-ordinate transformation given in 2.1, and map to fundamental domain Γ .

Step 3 Given the points in geostrophic space the weights which define the Laguerre cells in the physical domain are calculated using DA.

Step 4 The equations are now time stepped from the transformed momentum equations 2.5

$$\begin{aligned}\frac{DX_n}{Dt} - \frac{Cg}{f\theta_0}(\tilde{z}_n - H/2) &= 0 \\ \frac{DZ_n}{Dt} - \frac{Cg}{f\theta_0}(X_n - \tilde{x}_n) &= 0\end{aligned}$$

Where X_n, Z_n represent the geostrophic points at the current time step, and \tilde{x}_n, \tilde{z}_n represent the centroids of the Laguerre cells. In this project both a Forward-Euler scheme and Heun's method have been used for time-stepping.

Step 5 The geostrophic points are now replaced with X_{n+1}, Z_{n+1} and steps 3 and 4 are repeated until the final time is reached.

For the remainder of the report this numerical solver for 2.5 will be referred to as SG/DA.

4.2 Initialisation of Points in Geostrophic Space

Given a finite set of equidistant points in the physical domain Γ , the points are transformed to geostrophic space using

$$X = x + \frac{v_g}{f}, \quad Z = \frac{g\theta'}{f^2\theta_0} \tag{4.2}$$

This requires the form of θ' given by 1.14 from this v_g can be deduced using the following equations from 1.12,

$$\begin{aligned}\frac{\partial \varphi}{\partial z} - \frac{g\theta'}{\theta_0} &= 0 \\ \frac{\partial \varphi}{\partial x} - fv_g &= 0\end{aligned} \tag{4.3}$$

using the boundary condition $\int_0^H \varphi(x, z) dz = 0$ Integrating the first equation in z ,

$$\begin{aligned}\frac{\partial \varphi}{\partial z} &= \frac{g\theta'}{\theta_0} = N_0^2 z + \frac{Bg}{\theta_0} \sin\left(\pi\left(\frac{x}{L} + \frac{z}{H}\right)\right) \\ \varphi &= \frac{N_0^2 z^2}{2} - \frac{BgH}{\theta_0 \pi} \cos\left(\pi\left(\frac{x}{L} + \frac{z}{H}\right)\right) + F(x)\end{aligned}$$

Applying the boundary condition to determine $F(x)$,

$$\int_0^H \varphi dz = \left[\frac{N_0^2 z^3}{6} - \frac{BgH^2}{\theta_0 \pi^2} \sin\left(\pi\left(\frac{x}{L} + \frac{z}{H}\right)\right) + F(x)z \right]_0^H = 0$$

Using $\sin\left(\frac{\pi x}{L} + \pi\right) = -\sin\left(\frac{\pi x}{L}\right)$,

$$\begin{aligned}0 &= \frac{N_0^2 H^3}{6} - \frac{BgH^2}{\theta_0 \pi^2} \sin\left(\frac{\pi x}{L} + \pi\right) + \frac{BgH^2}{\theta_0 \pi^2} \sin\left(\frac{\pi x}{L}\right) + F(x)H \\ 0 &= \frac{N_0^2 H^3}{6} + \frac{2BgH^2}{\theta_0 \pi^2} \sin\left(\frac{\pi x}{L}\right) + F(x)H\end{aligned}$$

This gives $F(x)$ as,

$$F(x) = -\frac{N_0^2 H^2}{6} - \frac{2BgH^2}{\theta_0 \pi^2} \sin\left(\frac{\pi x}{L}\right)$$

and consequently φ as,

$$\varphi(x, z) = \frac{N_0^2 z^2}{2} - \frac{BgH}{\theta_0 \pi} \cos\left(\pi\left(\frac{x}{L} + \frac{z}{H}\right)\right) - \frac{N_0^2 H^2}{6} - \frac{2BgH}{\theta_0 \pi^2} \sin\left(\frac{\pi x}{L}\right) \quad (4.4)$$

Using the second of equations 4.3 v_g is found as,

$$v_g = \frac{BgH}{f\theta_0 L} \cos\left(\pi\left(\frac{x}{L} + \frac{z}{H}\right)\right) - \frac{2BgH}{f\theta_0 \pi} \sin\left(\frac{\pi x}{L}\right) \quad (4.5)$$

Together with θ' given by 1.14 this expression for v_g can be used to determine X and Z in geostrophic co-ordinates through the transform 4.2.

4.3 Choice of Initial Weights

The Laguerre diagram of this set of points shown in figure 4.1 with zero weights would define Laguerre cells exterior to Γ . These cells will have zero “mass” in the domain Γ . Physical intuition tells us that given the rigid lid and periodic boundary conditions points would physically not be able to leave the domain. However, thinking of fluid particles as the centroids of Laguerre cells, a cell outside the domain would represent a fluid particle on the exterior of the domain. This also poses

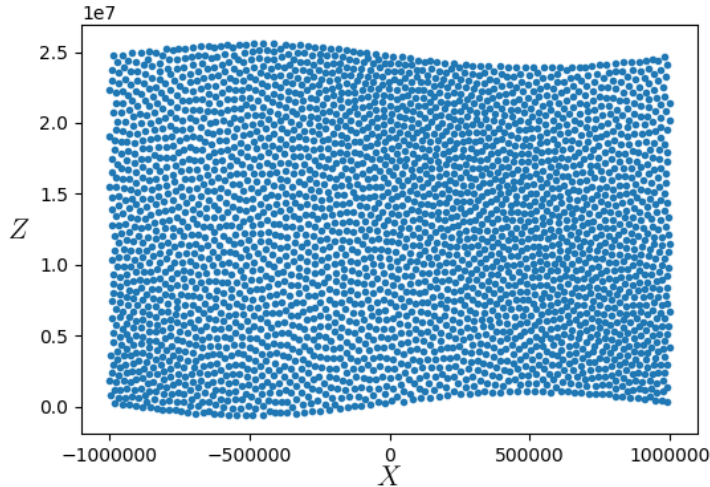


Figure 4.1: Plot of points in geostrophic space, transformed from a random set of points in $\Gamma := [-L, L] \times [0, H]$ using 2.1 with v_g as defined in 4.5

a problem with respect to the implementation of DA, as emphasised in [16], as it requires $\mu(\text{Lag}_{y_i}(\psi))$ to be a monotonic function of $\psi = (\psi(y_1), \dots, \psi(y_N))$ where N is the number of points initialised in Γ . According to [16] this occurs near points where the Laguerre cells contain positive mass over Γ .

Fortunately, a solution is provided in [16]. Proposition 25 in the paper proves that if the initial weights are given by,

$$\psi_i^0 = d(\mathbf{Y}_i, \Gamma)^2$$

where $\mathbf{Y}_i = (X_i, Z_i)$ are the points in geostrophic space. Since the domain is rectangular vertical distance from the point to the upper or lower boundary of the domain. The boundaries, given by $z = 0$ and $z = H$ are also perturbed to guarantee strict positivity of the mass of the Laguerre cells,

$$\psi_i^0 = \begin{cases} (Z_i - 0.9H)^2, & Z_i > 0.9H \\ (Z_i - 0.1H)^2, & Z_i < 0.1H \end{cases} \quad (4.6)$$

Comment: Address disparity with paper '-' sign - convention used in paper for finding Laguerre cells different to code? The Damped newton algorithm, DA, is initialised with the the geostrophic points and weights given by 4.6. The algorithm outputs weights that give Laguerre cells with equal mass over the periodic domain.

4.4 Time Stepping

Once the initial points and weights have been set up, it remains to find the geostrophic points at the next time step, using equations 2.5.

4.4.1 Forward-Euler Scheme

The numerical solution to equations 1.12 developed follows a Lagrangian framework, thus it is justified to treat the material derivative $\frac{D}{Dt}$ as a full derivative $\frac{d}{dt}$, in this sense we will develop prognostic scheme using the equations,

$$\begin{aligned}\frac{dX}{dt} - \frac{Cg}{f\theta_0} (\tilde{z} - H/2) &= 0 \\ \frac{dZ}{dt} - \frac{Cg}{f\theta_0} (X - \tilde{x}) &= 0\end{aligned}$$

Applying a Forward-Euler scheme [27] for time-stepping given by,

$$\begin{aligned}t^{n+1} &= t^n + h \\ Z_i^{n+1} &= Z_i^n + \frac{hCg}{f\theta_0} (X_i^n - \tilde{x}_i^n) \\ X_i^{n+1} &= X_i^n + \frac{hCg}{f\theta_0} (\tilde{z}_i^n - H/2)\end{aligned}\tag{4.7}$$

where $\tilde{x}_i^n, \tilde{z}_i^n$ represent the centroids of the Laguerre cells given by equations 4.8 using X_i^n, Z_i^n and corresponding weights given by the optimal transport algorithm (DA),

$$\tilde{x}_i^n = \frac{\int_{\text{Lag}_{Y_i^n}(\psi)} x \, dx dz}{\int_{\text{Lag}_{Y_i^n}(\psi)} dx dz}, \quad \tilde{z}_i^n = \frac{\int_{\text{Lag}_{Y_i^n}(\psi)} z \, dx dz}{\int_{\text{Lag}_{Y_i^n}(\psi)} dx dz}\tag{4.8}$$

Before the next iteration of the time-step the points X_i^{n+1}, Z_i^{n+1} are mapped back to the fundamental domain.

4.4.2 Heun's Method

For comparison and to test convergence the time-stepping was also implemented using Heun's method [27].

$$\begin{aligned}
 t^{n+1} &= t^n + h, & \hat{Z}_i^{n+1} &= Z_i^n + \frac{hCg}{f\theta_0} (X_i^n - \tilde{x}_i^n), & \hat{X}_i^{n+1} &= X_i^n + \frac{hCg}{f\theta_0} (\tilde{z}_i^n - H/2) \\
 Z_i^{n+1} &= Z_i^n + \frac{h}{2} \left(\frac{Cg}{f\theta_0} (X_i^n - \tilde{x}_i^n) + \frac{Cg}{f\theta_0} (\hat{X}_i^{n+1} - \hat{x}_i^{n+1}) \right) \\
 X_i^{n+1} &= X_i^n + \frac{h}{2} \left(\frac{Cg}{f\theta_0} (\tilde{z}_i^n - H/2) + \frac{Cg}{f\theta_0} (\hat{z}_i^{n+1} - H/2) \right)
 \end{aligned} \tag{4.9}$$

Where again, \hat{x}_i^n and \hat{z}_i^n represent the centroids of the Laguerre cells given using 4.8 and $\hat{X}_i^{n+1}, \hat{Z}_i^{n+1}$ with corresponding weights given by the optimal transport algorithm DA.

Comment: why not higher order time-step method? Limited by OT solver - 2nd order? **Comment: include map back to fundamental domain explanation and why this isn't done for centroids** A comparison of results using Heun's method and the forward-Euler scheme for timestepping is detailed in Chapter 5.

4.5 Visualising the Output

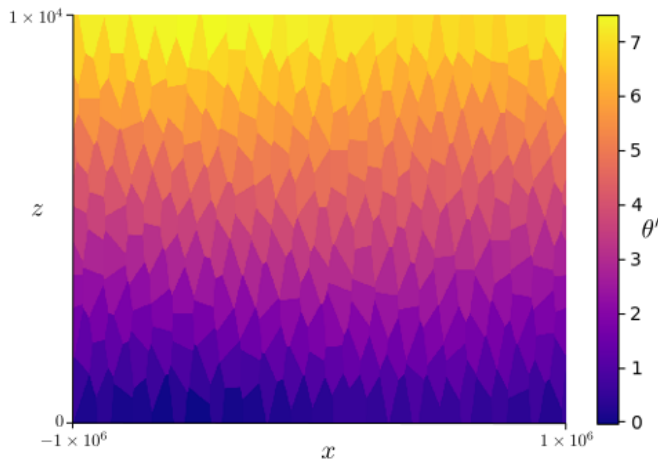


Figure 4.2: Laguerre Diagram of cells (24×12) found by finding the weights associated with the optimal transport of points initialised in geostrophic space to cells in the physical domain under the constraint of volume conservation. The cells are coloured according to the value of θ' given by the Z co-ordinate of the corresponding point in geostrophic space

Given the Geostrophic points and the associated weights which solve the optimal

transport problem a Laguerre diagram satisfying 3.2.1 can be constructed. In the Monge-Ampère library of DA [16, 5] the function ‘rasterization_2’ rasterizes a Laguerre diagram to a array of pixels of a specified size. The function ‘pcolormesh’ in the matplotlib is then used to visualise these results. To create this plot the periodic boundary conditions must again be considered carefully. This is done in a similar manner to the how they are treated for the application of DA. Copies of the points, weights and now colour values (in this case θ') are made and the ‘rasterization_2’ function is called with these inputs as well as the boundaries of the original domain.

Comment: inline code? For example, in the images below the Laguerre cells are coloured according to the value of θ' given by, $\theta' = \frac{f^2 \theta_0 Z}{g}$

Chapter 5

Numerical Simulations and Results

In this chapter we discuss the numerical results of the implementation of algorithm 4.1 using the PyMongeAmpere library [5] for solving the optimal transport problem. The use of this algorithm allows us to produce results with higher resolutions than previously realised. Plotting the Laguerre diagrams confirms the formation of a front as compared to similar results produced by [13, 17]. Finally, the validity of the numerical implementation is investigated and performance analysed to assert the suitability of the numerical implementation in providing a solution to equations 1.12.

5.1 Physical interpretation of Results

Using the plotting process described in section 4.5. The Laguerre diagrams below show snapshots of frontogenesis and the subsequent evolution of the front. The model was initialised with a grid of 80×40 points taken from an optimised sampling of points in the physical domain $\Gamma = [-L, L] \times [0, H]$ and transformed to geostrophic co-ordinates as explained in 4.2. This involves an application of Lloyd's algorithm where first moments of cells are iteratively found until points are equidistant in the domain. A summary of parameter values is given in table 5.1. For the following results Heun's method described in section 4.4.2 was used for time-stepping for a time period of 25 days from a randomly generated mesh.

In diagrams 5.1-5.2 we see the growth of the normal mode instability. Initially (a) the stratification of potential temperature, θ' is linear, as in the base state. By 2.5 (b) days we see the instability appear in the form of a wave and by 6 days a strong front has formed as a large gradient in θ' . We see that warmer air in the upper atmosphere has been come down into the lower regions of the atmosphere. By (d) the front has collapsed again as the normal mode instability loses its predominance.

Parameter	Value	Parameter	Value
L	$1 \times 10^6 \text{ m}$	H	$1 \times 10^4 \text{ m}$
g	10 ms^{-2}	f	10^{-4} s^{-1}
N^2	$2.5 \times 10^{-5} \text{ s}^{-2}$	θ_0	300 K
C	$3 \times 10^{-6} \text{ m}^{-1}\text{K}$	B	0.25 Ks^{-1}

Table 5.1: Table of parameter values used in numerical implementation of SG/DA as given by [3] with B chosen independently.

An interesting phenomenon observed after this is that the instability grows again and a secondary front is formed. A cycle then forms of an growing instability in one direction forming a front which is then dissipated and a subsequent instability grows in the opposite direction. Some snapshots of this cycle are shown in the images below. This cycle is due to the balance between the normal mode instability and the background shear. Initially the instability is free to grow dominating the dynamics and leading to frontogenesis. The vertical shear counterbalances the growth of the instability dissipating the front. Internal instabilities then act to contribute towards the growth of a new front, however this secondary front is not as strong. The vertical shear again acts to restore the system to its original state and the cycle continues like this.

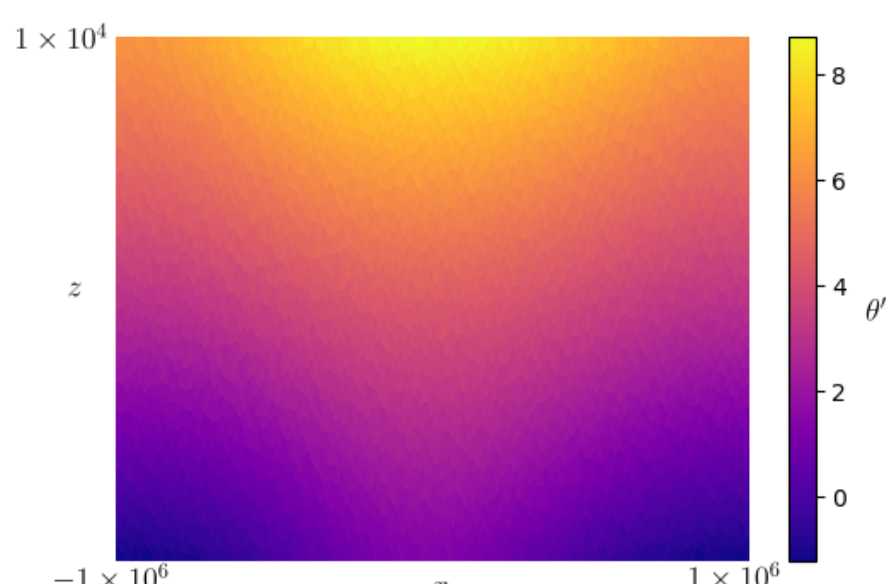
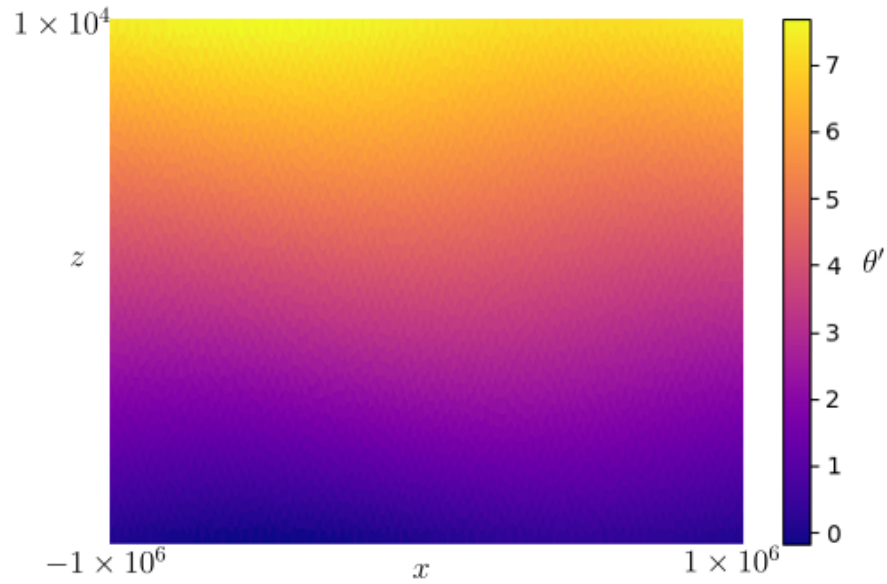
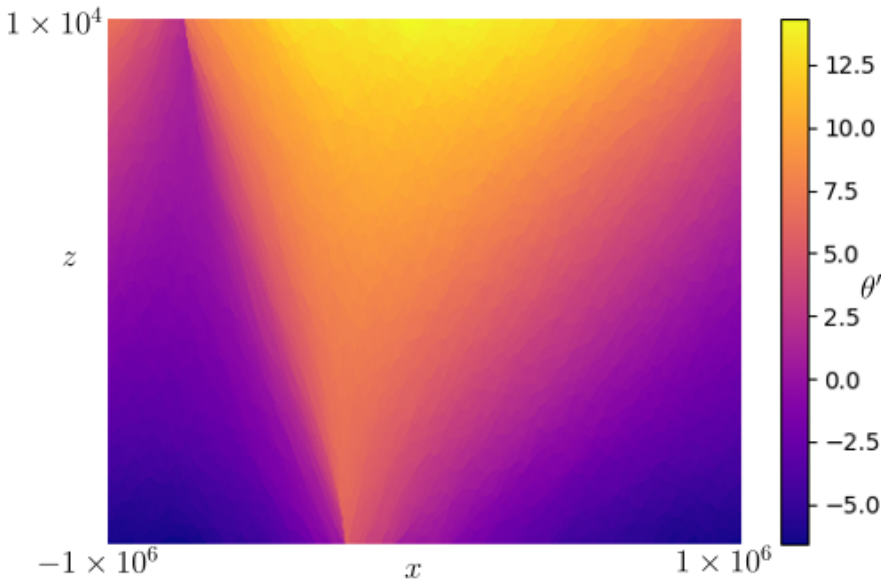
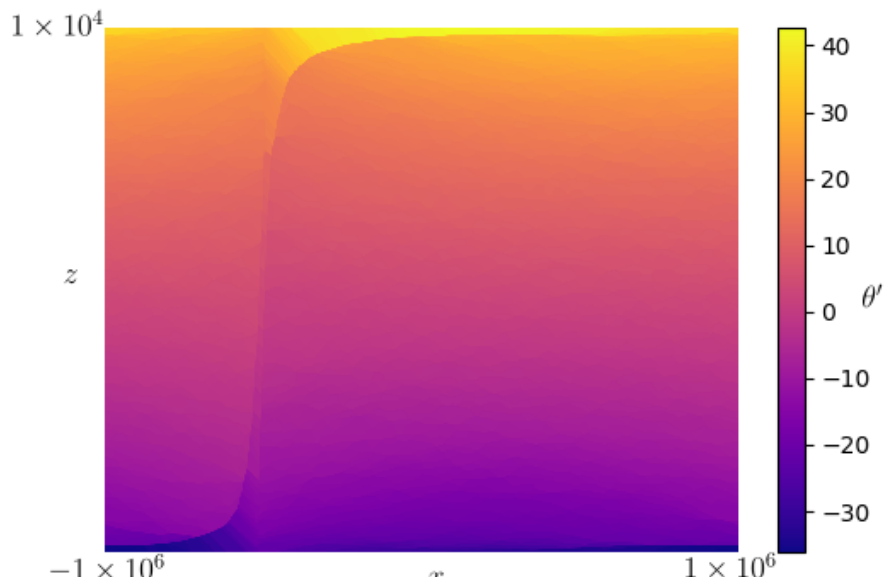


Figure 5.1: Plots of Laguerre Diagrams shaded according to the value of θ' using a random mesh of 80×40 points initialised in geostrophic space using 4.2 at (a) 0 days, (b) 2.5 days (c) 6 days and (d) 9 days, $\Gamma = [-L, L] \times [0, H]$, where $L = 1 \times 10^6$ and $H = 1 \times 10^4$



(a)



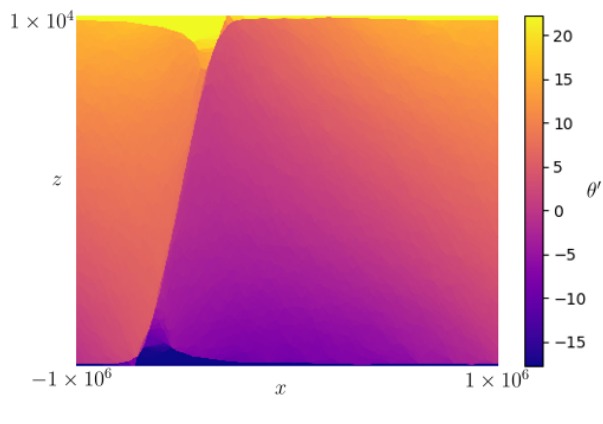
(b)

Figure 5.2: Plots of Laguerre Diagrams shaded according to the value of θ' using a random mesh of 80×40 points initialised in geostrophic space using 4.2 at (a) 6 days, (b) 9 days, $\Gamma = [-L, L] \times [0, H]$, where $L = 1 \times 10^6$ and $H = 1 \times 10^4$

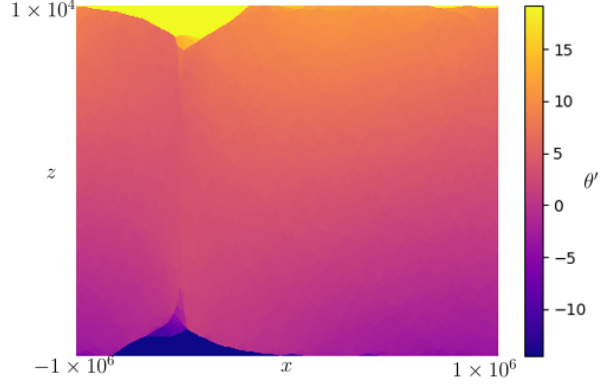
Diagram (a) in 5.3 shows the formation of the secondary front, (b) 5.3 in shows its collapse and (c) shows the formation of a third front with a reversed gradient in θ' . The front formation is not as clear in these images. The range in θ' has been reduced to half its original range to illustrate the cycle better. This leads to

a saturation of colour at the top and bottom of the Laguerre diagrams as extreme values of θ' are mapped to the end points of the scale. As suggested by Dr Cotter this could be due to outlying points which contribute to extreme values of θ' . This skews the colour range as seen in figure 5.3

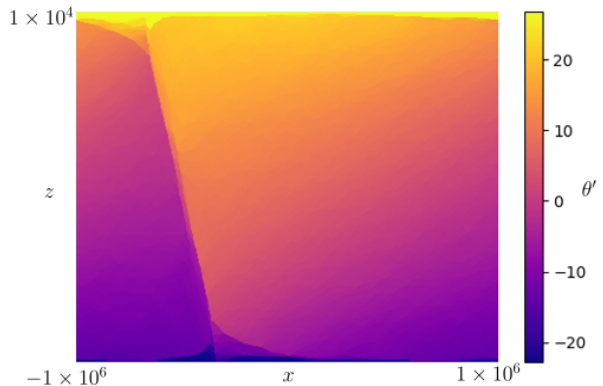
Another interesting visualisation of the result is that of using v_g the cross slice velocity as a colour scale. The diagrams below illustrate this for the same data as in figures 5.1, 5.2. The front formation is a lot clearer in this case especially for the cycle of front formation and collapse.



(a)



(b)



(c)

Figure 5.3: Plots of Laguerre Diagrams shaded according to the value of θ' using a random mesh of 80×40 points initialised in geostrophic space using 4.2 at (a) 11 days, (b) 12.5 days (c) 14.5 days, $\Gamma = [-L, L] \times [0, H]$, where $L = 1 \times 10^6$ and $H = 1 \times 10^4$

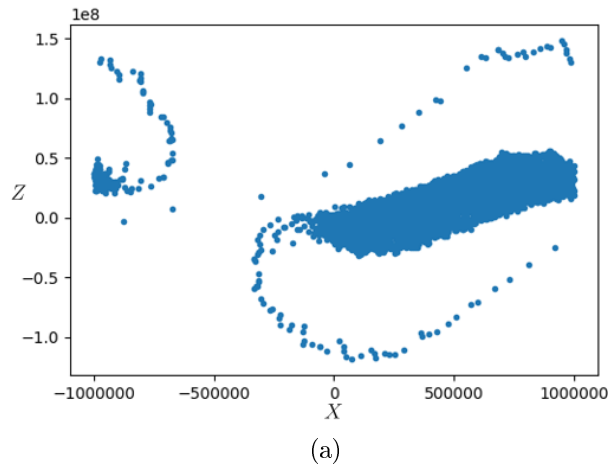


Figure 5.4: Plot of Geostrophic points at 11 days

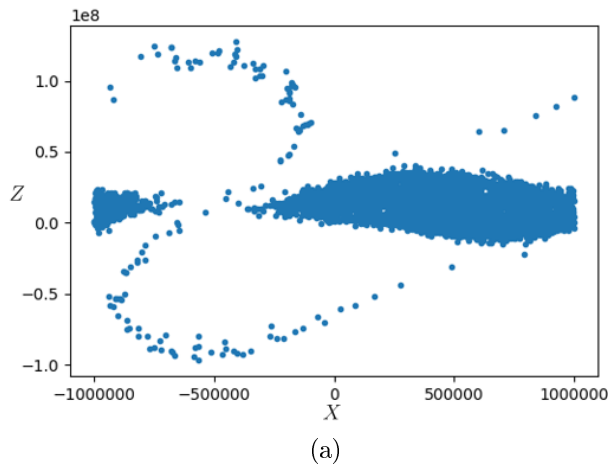


Figure 5.5: Plot of Geostrophic points at 12.5 days

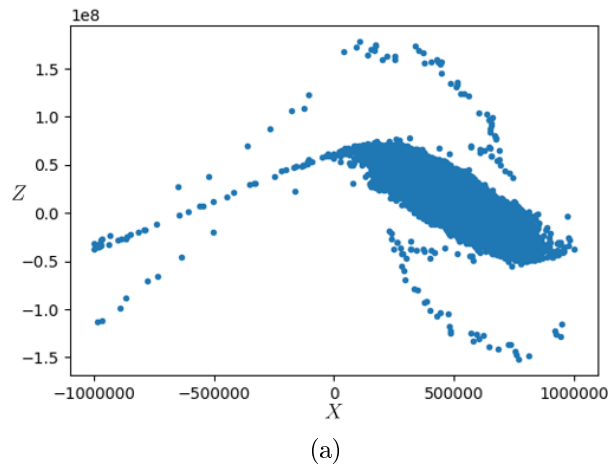
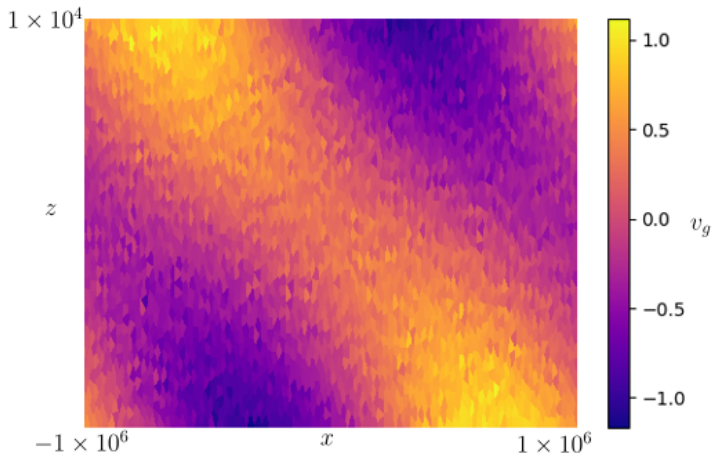


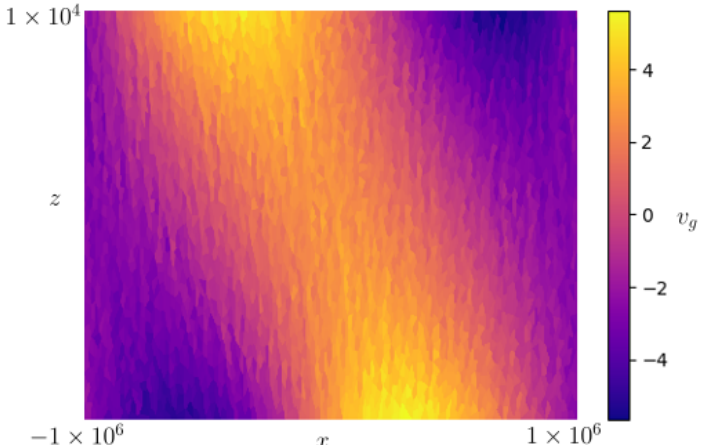
Figure 5.6: Plot of Geostrophic points at 14.5 days

5.2 Total Energy as a Measurement of Error

The aim of this section is to validate the results seen in section 5.1 above. With no known analytical solutions to the E₄₈ model for frontogenesis 1.12 that we



(a)



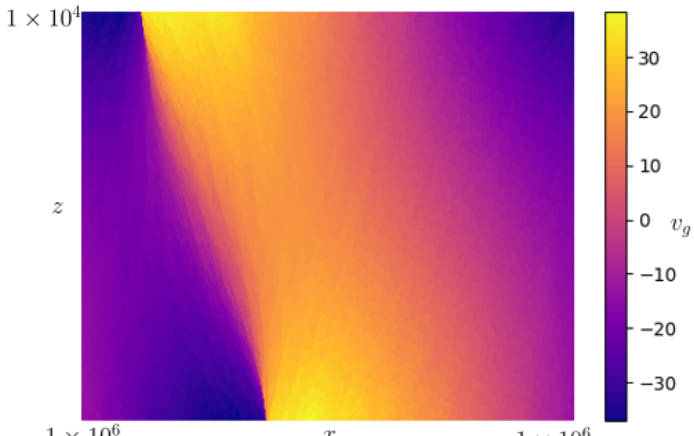
(b)

Figure 5.7: Plot of Laguerre Diagrams shaded according to the value of v_g using a random mesh of 80×40 points initialised in geostrophic space using 4.2 at (a) 0 days and (b) 2.5 days , $\Gamma = [-L, L] \times [0, H]$, where $L = 1 \times 10^6$ and $H = 1 \times 10^4$

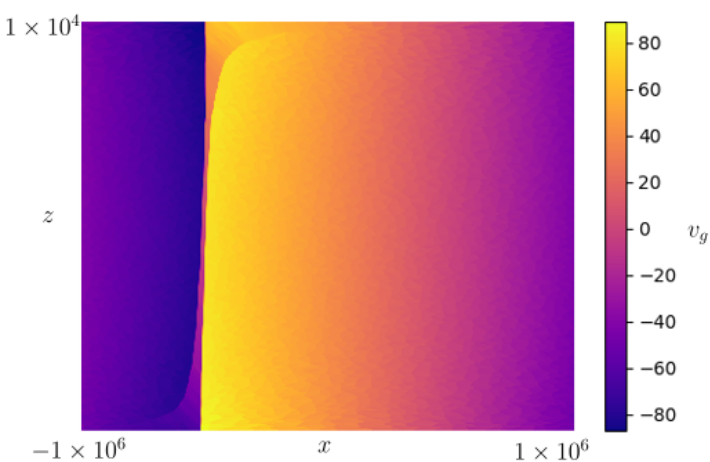
are studying and with no numerical models achieving the resolution we are able to achieve with SG/DA a challenge arises in how to confirm that the results are suitable solutions for the Semi-geostrophic Eady model. In this case, we turn to the total energy to quantify the error in the implementation. This is justified as we know from [3] that the total energy in equation 1.12 is conserved. However, given the form of total energy from 2.6 as,

$$E = f^2 \iint \frac{1}{2} (X - x)^2 - Z(z - H/2) dx dz \quad (5.1)$$

There is a clear dependence on the values of the points in geostrophic space and the values of the centroids of their corresponding Laguerre cells. This indicates a



(a)

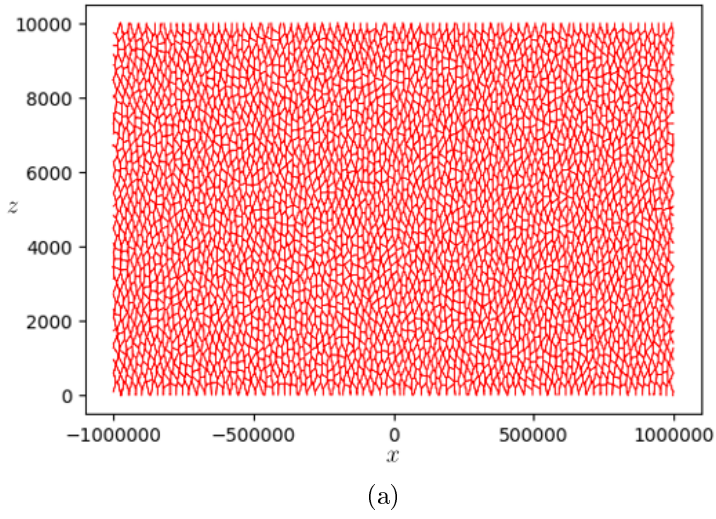


(b)

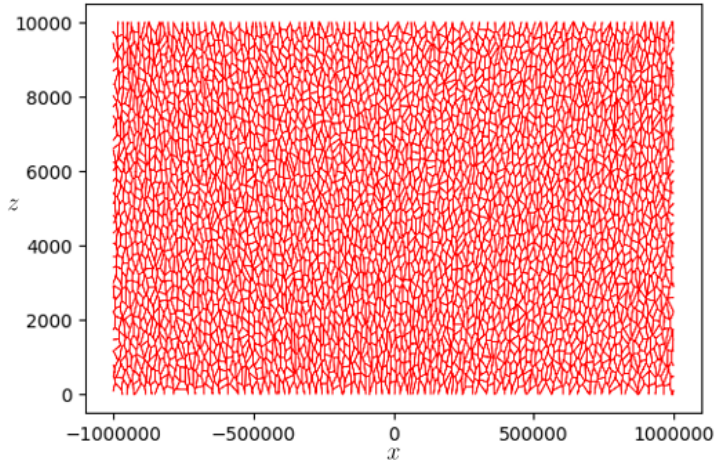
Figure 5.8: Plots of Laguerre Diagrams shaded according to the value of v_g using a random mesh of 80×40 points initialised in geostrophic space using 4.2 at (a) 6 days (b) 9 days $\Gamma = [-L, L] \times [0, H]$, where $L = 1 \times 10^6$ and $H = 1 \times 10^4$

dependence of the total energy of the system on the numerical solution given by SG/DA at each time-step. The graphs below show the total energy given by a system initialised from a grid of 80×40 points in geostrophic space (again from applying the transformation to points in physical space by 4.2). This time a regular mesh was used to ensure that the initial energy (E_0) was the same for each simulation.

The effect of decreasing the time step value was investigated for both the Forward Euler and Heun time stepping schemes. In the following plots the energy error, e_t is defined as $e_t = E_t - E_0$. The final energy error e_f is used to create log-log plots confirming the relationship between the time step used and the numerical error of



(a)



(b)

Figure 5.9: Plot of Laguerre Cells generated using a random mesh of 80×40 points initialised in geostrophic space using 4.2 at (a) 0 days and (b) 2.5 days , $\Gamma = [-L, L] \times [0, H]$, where $L = 1 \times 10^6$ and $H = 1 \times 10^4$

the implementation. What is most interesting in this is the gradient of the line of best fit, this gives an indication of the order of accuracy of the method. What we expect to see is a gradient, m , close to $m = 1$ for the Euler method as this is well known to have a linear rate of converge [27] and $m = 2$ for the Heun method as this has a quadratic rate of convergence [27].

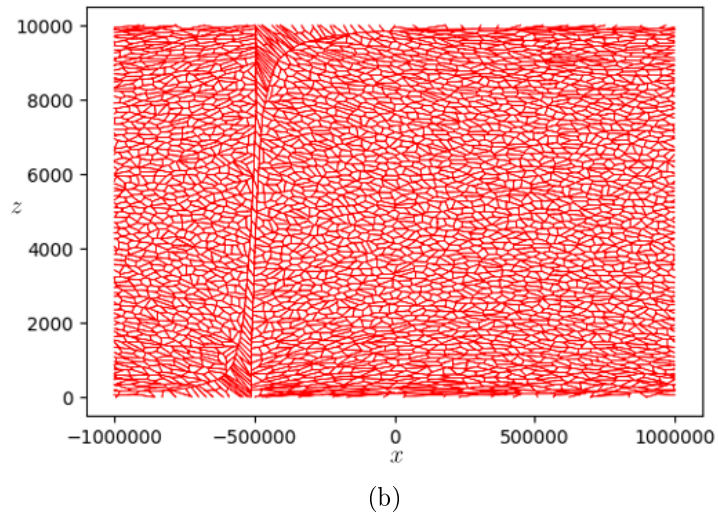
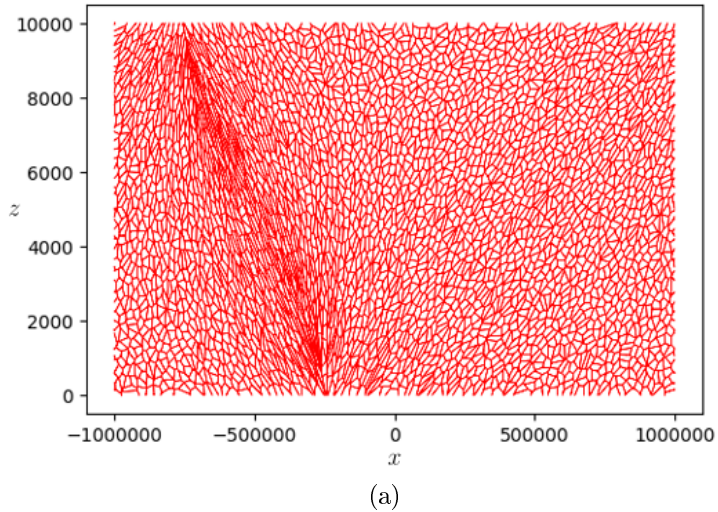
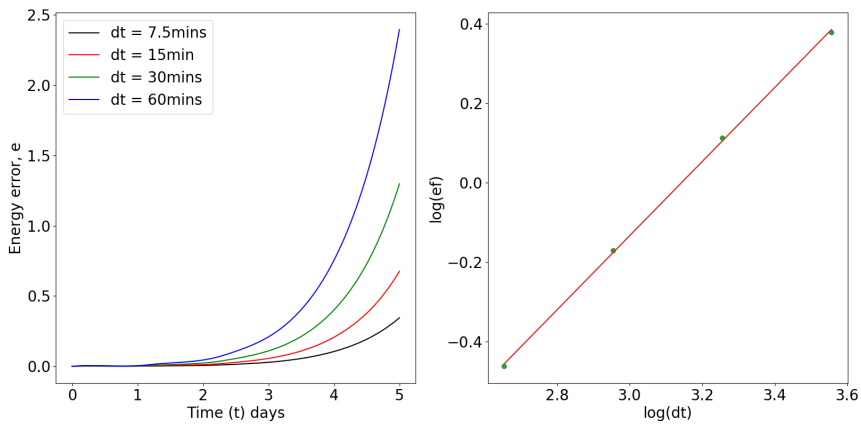


Figure 5.10: Plots of Laguerre Cells generated using a random mesh of 80×40 points initialised in geostrophic space using 4.2 at (a) 6 days (b) 9 days $\Gamma = [-L, L] \times [0, H]$, where $L = 1 \times 10^6$ and $H = 1 \times 10^4$

Figures 5.11 and 5.12 indicate promising initial findings. The straight lines in the log-log plots are clear evidence of a power law governing the error - time step relation. Moreover, the gradient values are reasonably close to what we were expecting.

The difference in computed values for the gradient to expected values is attributable to the error in applying the Damped Newton Algorithm in DA. To expand, rates of convergence are computed assuming $f(t, \mathbf{x})$ in $\frac{d\mathbf{x}}{dt} = f(t, \mathbf{x})$ has a Taylor expansion [27]. In the case of SG/DA the right hand side includes the implementation of DA which carries error associated with the Damped Newton Algorithm. This is particularly visible in the Heun implementation where the error is significantly smaller. In

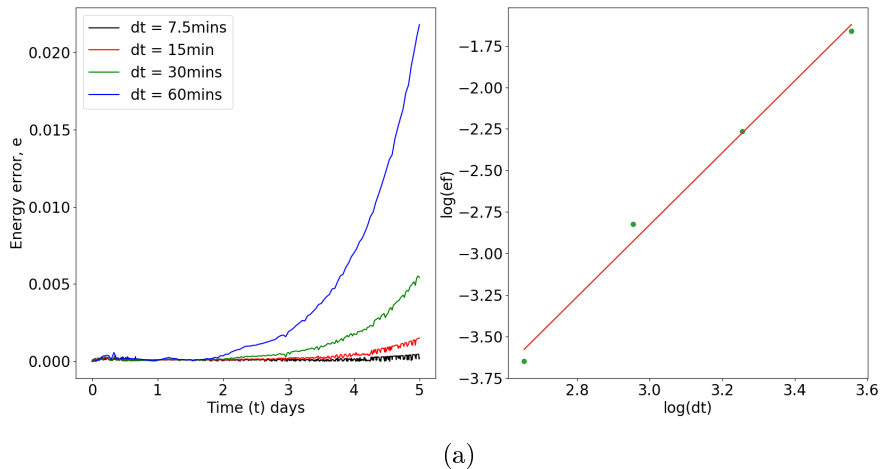


(a)

Figure 5.11: Energy error following the implementation of SG/DA with a Forward Euler time stepping method for 5 days on a regular mesh of 80×40 points. $\log(\Delta t)$ vs. $\log(e_f)$. The line of best fit has gradient $m = 0.933$, 3.s.f

this case the error associated with DA dominates that associated with the Heun's method and is seen as noise in the energy error curve.

Physically we can see that the energy error begins to grow the most between days 4 and 5, which coincides with the point where the front seen in figures 5.1,5.2 begins to grow most rapidly. To investigate this further the energy error is found for a period of up to 10 days.



(a)

Figure 5.12: Energy error following the implementation of SG/DA with a Heun time stepping method for 5 days on a regular mesh of 80×40 points. $\log(\Delta t)$ vs. $\log(e_f)$. The line of best fit has gradient $m = 2.17$, 3.s.f

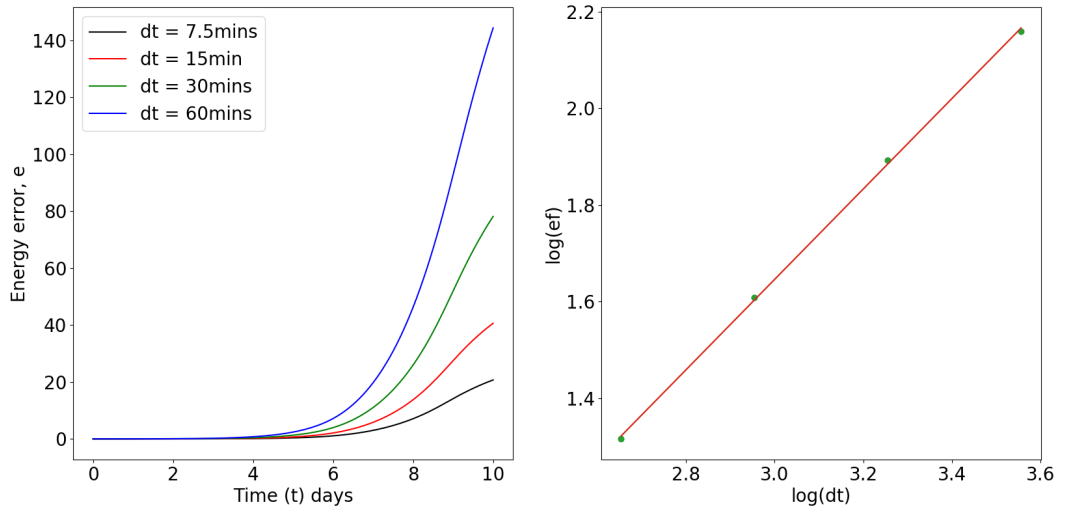


Figure 5.13: (a) Energy error following the implementation of SG/DA with a Forward Euler time stepping method for 10 days on a regular mesh of 80×40 points. (b) $\log(\Delta t)$ vs. $\log(e_f)$. The line of best fit has gradient $m = 0.935$, 3.s.f

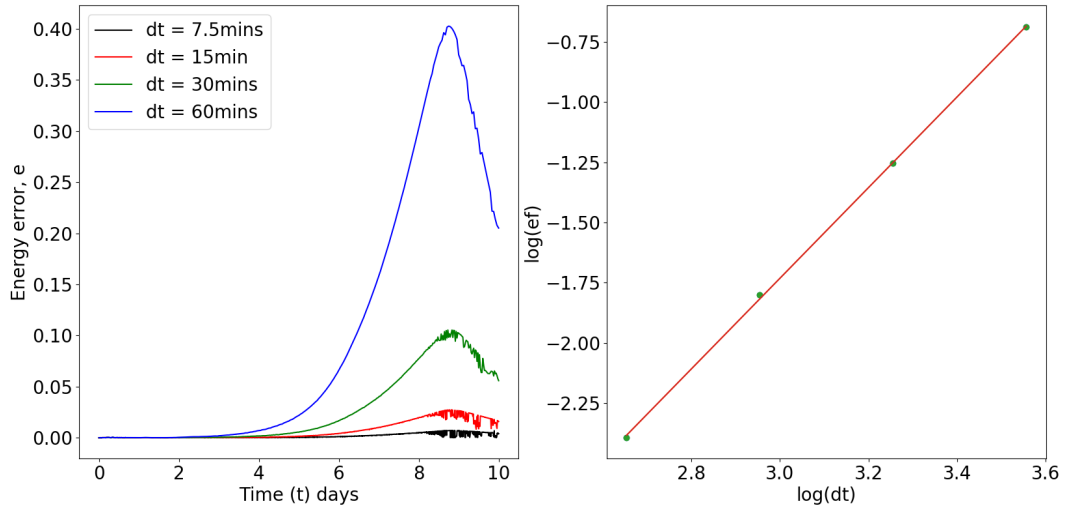


Figure 5.14: (a) Energy error following the implementation of SG/DA with a Heun time stepping method for 10 days on a regular mesh of 80×40 points.
(b) $\log(\Delta t)$ vs. $\log(e_f)$. The line of best fit has gradient $m = 1.88$, 3.s.f

5.3 A Comparison of Time Stepping Methods

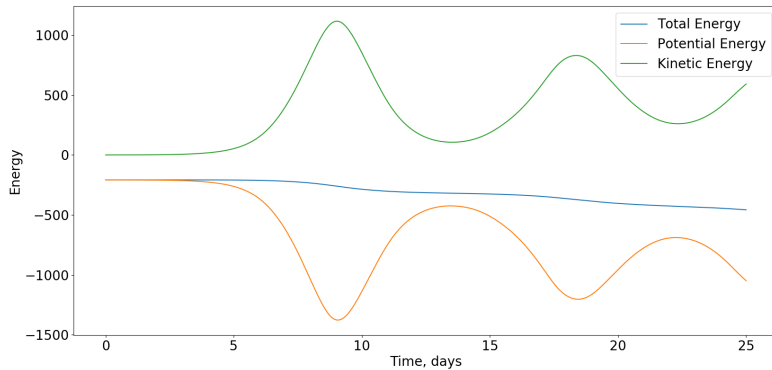


Figure 5.15: Energy evolution for SG/DA with Euler time step scheme for regular grid of initialised points

To validate the behaviour exhibited in section 5.1 we look at the behaviour of the Kinetic Energy, Potential Energy and Total Energy with time. We restate the energy in the form 2.6,

$$E = f^2 \iint \frac{1}{2} (X - x)^2 - Z(z - H/2) \, dx \, dz \quad (5.2)$$

The kinetic energy over the domain Γ is defined by,

$$E_{kin} = \int_{\Gamma} \frac{f^2}{2} (X - x)^2 \, dx \, dz \quad (5.3)$$

And the potential energy given by,

$$E_{pot} = \int_{\Gamma} -Z(z - H/2) dx dz \quad (5.4)$$

We now investigate the evolution of these quantities for a period of 25 days for each time stepping method, initialised with a regular mesh of 80×40 points transformed to geostrophic co-ordinates as in 4.2. In figure 5.15 the cycle of frontogenesis and collapse is much clearer seen in the periodic nature of the Kinetic energy. The graph also shows that energy dissipation in the Forward Euler method is strongest after front formation.

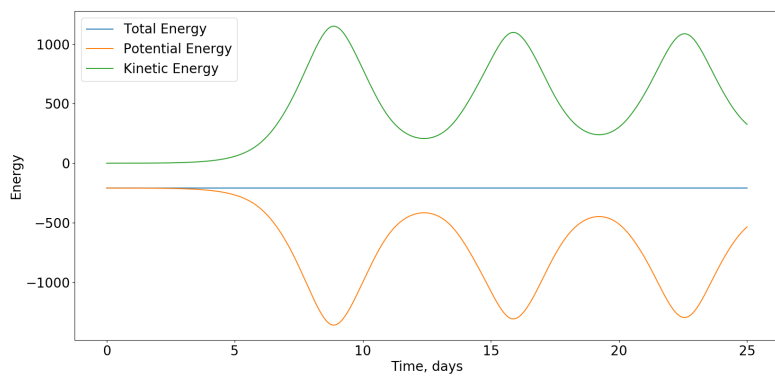


Figure 5.16: Energy evolution for SG/DA with Heun time step scheme for an initially regular grid of points

From figure 5.16 we see that Heun's method gives numerical results that appear to maintain energy conservation. Comparing the kinetic energy to that of the Forward Euler method there is significantly less damping in the cycle of front formation. The differences in behaviour of kinetic energy is explored further in 5.17.

The comparison in figure 5.17 shows a significant damping in the amplitude of oscillations in the Forward Euler time stepping scheme compared to the Heun scheme, where the second oscillation appears slightly damped but the third very similar in amplitude to the second. What is also striking is the difference in the periods of oscillation. The period of oscillation in Heun's method is significantly smaller and more uniform indicating a dispersion error in the Forward Euler implementation.

Comment: [3]period of oscillation

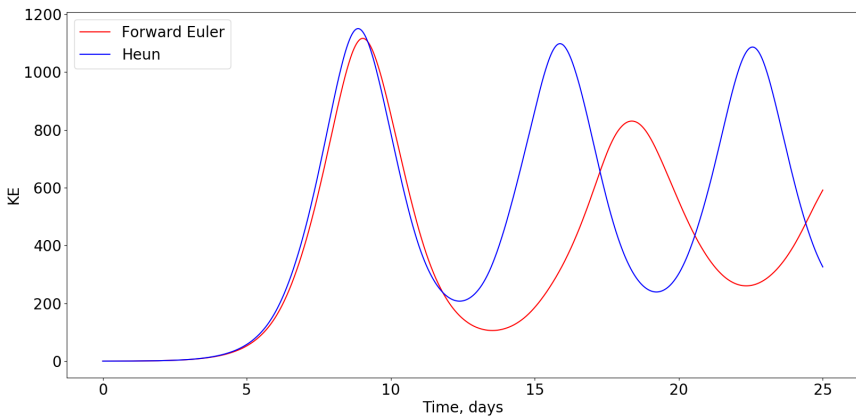


Figure 5.17: Comparison of energy evolution of solution of SG/EM with SG/DA for Heun and Forward Euler time-stepping schemes over a period of 25 days with a regular grid of initial points

5.4 Computational Performance

The results of sections 5.3 and 5.2 show a clear indication that using Heun's method for the time stepping of SG/DA gives a significantly more accurate result. However, considering that to implement Heun's method requires two calls to DA to solve the optimal transport problem at the prediction stage and correction stage the benefit of extra accuracy could be lost in a large increase to the runtime of the algorithm. Due to this we would expect the runtime of Heun's method to be close to twice that of Euler's method. In this section we investigate the additional time cost to running Heun's method in time stepping and evaluate whether this is justified.

N , ($2N^2$ points)	Runtime (s) FE Method	Runtime (s) Heun Method
30	40.430	81.479
35	59.898	114.232
40	93.374	179.741
45	148.440	274.582
50	200.886	372.805
55	286.968	503.502
60	410.417	663.437

Table 5.2: A comparison of runtime (seconds) by Forward Euler and Heun's time step methods using python cProfile package

To compare the runtime of each time stepping method the python package cProfile was used around the time iteration part of the algorithm. Of course, this means that some set-up time costs are factored into the runtime measurement. From table 5.2 it is already evident from table that the runtime of Heun's method is significantly greater than that of the Forward Euler method. Whilst for smaller values of N the

runtime is approximately doubles between implementing Euler and Heun's method we see that above $N = 45$ this relationship deteriorates.

To analyse this further we visualise the data from 5.2 by plotting a best fit line for each method by linear regression using the ‘scipy.stats’ package available in python.

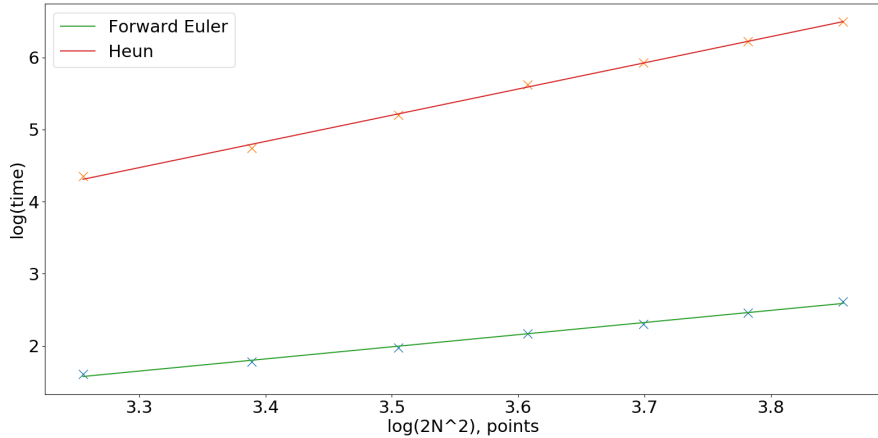


Figure 5.18: Logarithmic plot showing $\log(2N^2)$ vs $\log(\text{runtime})$ for $N = (30, 35, 40, 45, 50, 55, 60)$ as in table 5.2 and line of bestfit. The gradient of the line of bestfit for the Forward Euler method is 1.68 3.s.f and for 3.63 3.s.f for Heun's method using runtimes from 5.2

Figure 5.18 highlights this disparity observed in the table we see that the gradient in the line of best fit of Heun's method is in fact 2.16 times that of the Forward Euler method. Indicating another source of time cost in Heun's method. There are a number of reasons this could be. The additional time step calculation for the correction step of Heun's method would contribute to the increase in time cost.

From the cProfile results, which can be seen from running ‘SG_DA_performance.py’ (in the sg_monge_ampere repository) that the greatest time cost is in running DA to solve the optimal transport problem. This runtime could be reduced by recycling the weights from the previous time step as an initial guess for DA in the following time step. In practice this is harder to implement as the time stepping moves points in geostrophic space in the Z direction. This means that the necessary condition for convergence, that the area of the cell associated with each geostrophic point is positive over the domain Γ is not necessarily satisfied. Therefore the initial guess given by 4.3 must be used for each call to DA. As the initial guess is most likely far from the final values of the weights this will greatly increase the time for DA to converge. As this is called twice in Heun's method this represents an additional

cost to runtime which is not so easily quantified. A possible remedy for this is to perturb the values for the weights from the previous time step in such a way that the condition for initial positive cell area is satisfied. However, this is a non trivial problem.

Conclusion

In the first part of this project we brought together the results of [1, 2, 3] in developing the framework for studying the process of frontogenesis through by applying the Eady model for the growth of baroclinic instability to the semi-geostrophic equations. The instability was introduced through a perturbation to the background potential temperature θ' . By transforming to geostrophic co-ordinates we saw how the SG equations could be written in a form in which the ageostrophic velocity was described implicitly.

Analysing work by Cullen [3], the need for an inverse transformation drove the solution towards that of a Monge-Ampère equation. This was finally shown to be an optimal transport problem minimising the energy 2.6. Lemma 2.2.2 showed this minimisation to be equivalent to that of minimisation of a quadratic cost function. In this form the problem was shown to be analogous to the problem solved by Kitagawa et al. in [4] with DA [5].

Using this framework we developed the equations in the form of a semi-discrete optimal transport problem finding the weights associated with the optimal transport map that takes cells in physical space to points in geostrophic space, under the constraint that the source and target domains have associated uniform probability densities. The use of continuous and discrete uniform probability densities satisfies the volume conservation condition Monge-Ampère formulation of SG.

Initial results in the form of plots of θ' over the domain Γ were consistent with what had been previously observed in simulations by [17, 13]. Namely frontogenesis was clearly observable between days 5 and 6 and the cycle of front formation and collapse observed by other simulations was observed. This was a clear indication that the use of DA for solving equations 1.12 was successful.

In the absence of analytical solutions for the model studied we undertook an analysis of error by means of studying the total energy of the system. Since the governing equations were known to be energy conservative [3] numerical error in the algorithm

could be quantified. Results were promising as they showed the rate of convergence to be consistent with what was expected for each time stepping method used, order 1 and 2 for the Forward Euler and Heun scheme's respectively. Moreover, the implementation of Heun's method in time stepping was shown achieve results close to conserving energy in the system, indicating improvements on previous results achieved by [17, 13].

A possible extension to this work could be implementing an implicit time stepping method. This would require a way to apply Newton's algorithm to solve for geostrophic points at subsequent time steps. In particular, a way to characterise the gradient of the right hand side of the time evolution of equations 2.5 will need to be found. This is non-trivial as the x, z are functions of X, Z found by the optimal transport algorithm.

Finally the performance of SG/DA with each time stepping method was investigated. The results for runtime were not as close to the predicted results as expected, that the runtime would be increased by a factor of two by implementing Heun's method. Heun's method exhibited run times that were significantly greater than the Forward Euler implementation. On further consideration this could be attributed to factors that convoluted the application of the optimal transport algorithm DA and the time stepping method. Most notably, the need to initialisation of weights to satisfy convergence criteria for DA.

To conclude, the solution of the model 1.12 through the use of the DA algorithm for optimal transport shows a clear convergence to a solution in both time stepping methods implemented. Although the efficiency of using Heun's algorithm for time stepping in the algorithm for solving 1.12 is reduced the indisputable difference in result and reduced error demonstrated by this implementation make it the obvious candidate for use in practice.

Appendix A

First Appendix

Bibliography

- [1] Brian J. Hoskins. The Geostrophic Momentum Approximation and the Semi-Geostrophic Equations. *Journal of the Atmospheric Sciences*, 32(2):233–242, 1975.
- [2] G. J. Shutts and M. J. P. Cullen. Parcel Stability and its Relation to Semi-geostrophic Theory. *Journal of Atmospheric Sciences*, 44:1318–1330, may 1987.
- [3] Michael J P Cullen. *A Mathematical Theory of Large-scale Atmosphere/ocean Flow*. Imperial College Press, jan 2006.
- [4] Jun Kitagawa, Quentin Mérigot, and Boris Thibert. Convergence of a Newton algorithm for semi-discrete optimal transport. 2016.
- [5] Quentin Mérigot. PyMongeAmpere, python, 2017.
- [6] Brian Golding, Kenneth Mylne, and Peter Clark. The history and future of numerical weather prediction in the Met Office. *Weather*, 59(11):299–306, nov 2004.
- [7] Antje Weisheimer. Antje Weisheimer Exploring and extending the limits of weather predictability?
- [8] B J Hoskins. The Mathematical Theory of Frontogenesis. *Annual Review of Fluid Mechanics*, 14(1):131–151, 1982.
- [9] Hiroe Yamazaki, Jemma Shipton, Michael J.P. Cullen, Lawrence Mitchell, and Colin J. Cotter. Vertical slice modelling of nonlinear Eady waves using a compatible finite element method. *Journal of Computational Physics*, 343:130–149, aug 2017.
- [10] Mike J.P. Cullen. A comparison of numerical solutions to the Eady frontogenesis problem. In *Quarterly Journal of the Royal Meteorological Society*, volume 134, pages 2143–2155. Wiley-Blackwell, oct 2008.
- [11] Richard Rotunno, William C. Skamarock, and Chris Snyder. An Analysis of Frontogenesis in Numerical Simulations of Baroclinic Waves, dec 1994.

- [12] Noboru Nakamura. Scale Selection of Baroclinic Instability - Effects of Stratification and Nongeostrophy. *Journal of Atmospheric Sciences*, 45:3253–3267, 1988.
- [13] N. Nakamura. Nonlinear Equilibration of Two-Dimensional Eady Waves: Simulations with Viscous Geostrophic Momentum Equations. *Journal of the Atmospheric Sciences*, 51:1023–1035, 1994.
- [14] E T Eady. Long Waves and Cyclone Waves. *Tellus*, 1(3):33–52, 1949.
- [15] B. J. Hoskins and F. P. Bretherton. Atmospheric Frontogenesis Models: Mathematical Formulation and Solution. *Journal of the Atmospheric Sciences*, 29(1):11–37, jan 1972.
- [16] Quentin Mérigot, Jocelyn Meyron, and Boris Thibert. An algorithm for optimal transport between a simplex soup and a point cloud. 2017.
- [17] M. J.P. Cullen and I Roulstone. A geometric model of the non-linear equilibration of two-dimensional Eady waves. *Journal of the Atmospheric Sciences*, 50:328–332, 1993.
- [18] Met Office. Weather Fronts, 2018.
- [19] Met Office. Surface Pressure Charts, 2018.
- [20] A. Eliassen. On the vertical circulation in the frontal zones. *Geofysiske Publikasjoner*, 4(4):147–160, 1962.
- [21] James C (UCLA) McWilliams. Fundamentals of Geophysical Fluid Dynamics. page 283, 2011.
- [22] Peter R. Bannon. Linear Baroclinic instability with the Geostrophic Momentum Approximation. *Journal of Atmospheric Sciences*, feb 1988.
- [23] William Blumen. A Semigeostrophic Eady-Wave Frontal Model Incorporating Momentum Diffusion. Part I: Model and Solutions. *Journal of the Atmospheric Sciences*, 47(24):2890–2902, dec 1990.
- [24] Yann Brenier and Mike Cullen. Rigorous derivation of the x-z semigeostrophic equations. *Communications in Mathematical Sciences*, 7(3):779–784, 2009.
- [25] J.-D. Benamou and Y. Brenier. Weak existence for the semigeostrophic equations formulated as a coupled Monge-Ampère/transport problem. *SIAM J. Appl. Math.*, 58(5):1450–1461, oct 1998.
- [26] Walter Rudin. *Real And Complex Analysis*. McGraw-Hill, 1986.

- [27] David F. Griffiths and Desmond J. Higham. *Numerical Methods for Ordinary Differential Equations*, volume 79. 2010.